Stoichiometric dependence and laser heating effect on the luminescence thermometric performance of Er^{3+}, Yb^{3+}: $Y_uGd_wVO_4$ microparticles in the non-saturation regime

Nisrin Mohamed Bhiri [1,2,*], Mohamed Dammak [1], Joan Josep Carvajal [2,*], Magdalena Aguiló [2] Francesc Díaz [2] and Maria Cinta Pujol [2]

[a]Université de Sfax, Laboratoire de Physique Appliquée, Groupe de Physique des matériaux luminescents, Faculté des Sciences de Sfax, Département de Physique, BP 1171, Université de Sfax, 3018 SFAX, Tunisie.
[b]Universitat Rovira i Virgili, Departament de Química Física i Inorgànica, Física i Cristal·lografia de Materials i Nanomaterials (FiCMA-FiCNA)
Marcel·li Domingo 1, Tarragona, 43007, Spain.
*E-mail : nesrine.bhiri@estudiants.urv.cat
joanjosep.carvajal@urv.cat

ABSTRACT

The performance of $Y_uGd_wVO_4$ microcrystals with different atomic concentrations of Y^{3+} and Gd^{3+} ions, co-doped Er^{3+} -Yb^{3+} , as thermometers, exploiting two different calculation methods based on the fluorescence intensity ratio is investigated in the non-saturation regime. At a low excitation power density of 20 W cm^{-2}, the thermometric parameters are approximately the same for all the analyzed sensors. Whereas for an excitation power density of 155 W cm^{-2}, they are widely different all along the 303-513 K temperature range of study. Such as an increase on the Gd^{3+} ion concentration in the microcrystals induces a lattice expansion that can result in the decreasing of the lattice field surrounding the Er^{3+} ions and then it could enhance greatly the thermometric performances. For both calculation methods, it has been demonstrated that the ΔE_{FIR} (fitted from the FIR curves) and the ΔE^{TS} (determined using the TeSen Calculator program) values are lower than the ΔE` experimental (fitted from the emission spectra measured at room temperature), whenever the sample is heated and then the thermometric parameters are less competitive.

Keywords: Er^{3+}/Yb^{3+}: $Y_uGd_wVO_4$, fluorescence intensity ratio, stoichiometry, laser heating, non-saturation regime.

1. Introduction

The temperature is a very important unit in thermodynamics. It is the most commonly measured physical parameter in science, industries, and life activities. In particularly, it is necessary to be determined for biological and technological applications, such as measuring the temperature of microfluidics and microcircuits, to name a few [1-2]. Thus, it is well advanced to monitor it during material processing for controlling the quality of the final products as well as in biomedical areas, where temperature provides basic diagnostic criteria [3-4]. The precise of measuring it for materials has a major impact on both scientific research and practical production. Recent years have seen the rise of luminescent temperature sensors (T-sensors) based on active rare earth (RE) doped materials which is a topic of scientific research and practical production owe to its extensive applications in different fields [5-8]. These non-contact luminescent thermometry could provide fast response, good accuracy, high spatial resolution, and tunable size in comparison with the traditional thermal sensing methods (invasiveness and big sizes) [9-11]. To measure the temperature of a distant object [12], the change in the luminescence properties of the active ion in a particular host matrix is recorded as a function of temperature.

Based on temperature-dependent luminescence parameters, such as the change in the relative intensities of different emission bands, the change in their polarization, the spectral position, the narrowing of the bands and the lifetime [10], various luminescent variations can be detected to

correlate them with the active material temperature and calibrate the T-sensor accordingly. Among the luminescent temperature sensing methods, the extremely promising and the most widely used one is based on the fluorescence intensity ratio (FIR) technique, where a two thermally coupled levels (TCLs) of triply charged lanthanide (Ln^{3+}) ions are essential to calibrate the optical response of the T-sensor [12,13-18]. Such as the energy gap, ΔE, separating these level pairs must be large enough to avoid strong overlapping of the two emissions ($>$ 200 cm^{-1}) and, in meanwhile, short enough ($<$ 2000 cm^{-1}) to enable the upper level to have a minimum population of Ln^{3+} ions in the temperature range of interest [19]. Therefore, the energy gap between those two TCLs must be, at certain temperatures, of the same order of magnitude as the thermal energy ($\Delta E \sim k_B T$ being k_B the Boltzmann constant and T, the temperature) to guarantee the population of the upper level following a simple Boltzmann distribution where the emission intensities of these thermalized levels strongly depend on temperature [12,13-14,20]. Hence, this method allows determining temperature via analysis of the emission intensity ratio between two TCLs without influences of the fluorescence losses and fluctuation of excitation intensity. Then, it can provide accurate fluorescent intensity measurements which leads to better temperature calibration performance [21-25].

Several Ln^{3+} ions such as Eu^{3+}, Ho^{3+}, Nd^{3+}, Pr^{3+}, Sm^{3+} and Er^{3+} have energy level pairs which satisfy the above criteria and have been widely used in optical T-sensors [12,14]. However, Er^{3+} ion is the most used Ln^{3+} ion for this application [14]. Representatively, Er^{3+} ion can emit green light at around 18500 cm^{-1} (~550 nm) under 980 nm excitation [26], Yb^{3+} ion generally absorbs 980 nm photons and enhances emission intensities of Er^{3+} ions as sensitizer [27-28]. And the Er^{3+} ion which includes TCLs, $^2H_{11/2}$ and $^4S_{3/2}$ with a small energy gap of around 800 cm^{-1} [29-30], is appropriate for FIR technique with preferable sensitivity and accuracy [31-32].

Recently, many papers in the literature dealing with optical T-sensors reported that the outstanding properties of host materials that contain structure, cut-off phonon energy, thermal/chemical stability and functionality determine the exploring ranges and temperature sensitivities of optical T-sensors based on the FIR technique [14,33-35]. Several successful applications rely on the FIR technique using green anti-Stokes emissions from Er^{3+} ions ($^2H_{11/2}$ and $^4S_{3/2}$ TCLs) have been extensively explored and the host materials are mainly vanadate matrices [36-38].

According to the conventional opinion, with taking into consideration the expression of the relative sensitivity $S_r = \Delta E/k_B T^2$, where ΔE is the energy separation between the two emitting states involved [14], the TCLs of Er^{3+} ions must own the similar relative sensitivity values. It must be stressed that it is strictly right when the electronic population between the two TCLs is strictly governed by the Boltzmann distribution law. However, a lot of pioneering works carried out by Marciniak *et al.*, as well as other groups, proved that there are several physical effects that can influence on the luminescence thermometry [26,39-33]. Then, it must be stated here that in the real scenario, multiple factors, including the dopant concentrations, the excitation intensity and regimes, the nano or micro thermometers crystal quality and particle size, multiphoton non-radiative processes, among others, are expected to impose an impact on the real luminescence intensity ratio, and thus on the actual thermal sensitivity [22,44-45].

In our previous works, we have reported that the 1 at. % Er^{3+}, 20 at. % Yb^{3+}: $GdVO_4$ microcrystals (MCs) operated under anti-Stokes emission process have the best thermal sensitivity with the value of 1.20 % K^{-1} at 303 K among all the prepared RE vanadate compounds [28]. Moreover, we have demonstrated that, for the same sensitizing matrix, the excitation laser power has an effect on the final thermal sensitivity to a large extent. And the temperature sensing based on the FIR technique can be improved with exciting at low excitation laser powers [46]. Great efforts are still underway in the development of these optical sensing materials with high sensitivity. As known, the optimization of the thermal sensitivity relies mostly on the most appropriate matrix, and the selection of a suitable host material, is crucial to enable the lower probability of non-radiative processes and to optimize the performance of optical thermometer. Then, herein, we use different concentrations of Y^{3+} and Gd^{3+} ions in the vanadate host matrix 1 at. % Er^{3+}, 20 at. % Yb^{3+}: $Y_uGd_wVO_4$ to compare their sensing behaviors, and further discuss the concentration effects on the FIR technique and the excitation power density impacts on the relative thermal sensitivity of the thermometric sensors. Also,

we will compare the calculation of the FIR by a program written on Matlab software that was already used and tested for determining the thermometric abilities of materials with a classical calculation using OriginLab@software. We will explore it for our developed compounds with presenting a comparison with the manual method used usually to determine the thermometric performance of materials.

2. Experimental section

Synthesis of luminescent Er^{3+}, Yb^{3+} co-doped $Y_uGd_wVO_4$ microcrystals.

MCs of 1 at. % Er^{3+}, 20 at. % Yb^{3+} co-doped $Y_uGd_wVO_4$ (u and w being the atomic concentrations of Y^{3+} and Gd^{3+} ions inserted in the co-doped $Y_uGd_wVO_4$ rare earth vanadate host; (u, w) = (0.79, 0), (0.5, 0.29), (0.29, 0.5) and (0, 0.79)) were synthesized through a simple high temperature solid-state reaction. The used precursors and materials even the method of synthesis have been fully detailed in our previous works [28,46]. In brief, the chemical precursors, in a stoichiometric mixture, after being grinded and mixed carefully, were submitted to a thermal treatment at a constant temperature of 1173 K for 6 hours in a conventional oven under ambient atmosphere.

Apparatus.

The powder X-ray diffraction (XRD) patterns of the prepared compounds were recorded on a Bruker AXS D-8 Advance diffractometer equipped with a Cu Kα radiation source (λ = 1.5406 Å), operating at 40 kV and 40 mA. Sample morphologies were observed with an environmental scanning electron microscopy (SEM, FEI QUANTA 600).

The vibration modes of the samples were analyzed at room temperature (RT) using PERKIN-ELMER-983 G Fourier transform infrared (FT-IR) spectrometer in the range of 400-4000 cm^{-1}.

Anti-Stokes RT emission of the Er^{3+}, Yb^{3+} co-doped $Y_uGd_wVO_4$ MCs were measured using a homemade luminescence microscope setup. The excitation of the samples was carried out with an Apollo Instruments Inc. diode laser with emission at 980 nm and a variable power density values in the 20-445 W cm^{-2} range. A microscope objective with 20x magnification and 0.40 numerical aperture was used to focus the laser beam on the samples. The emission was collected by the same microscope objective, and it was sent to an optical spectrum analyzer (OSA) Yokogawa AQ6373 to be recorded with a resolution of 10 nm and an integration time of 10 s. The scattered excitation radiation was eliminated by using a 750 nm short pass dichroic filter (Thorlabs). The measurements of the temperature-dependent anti-Stokes emission were performed using the same equipment where the MCs were placed in a heating stage (Linkam, THMS 600) in which the temperature is measured by a thermocouple with a temperature resolution of 0.1 K. All the measurements of the temperature-dependent anti-Stokes emissions were made every 10 K from 303 to 513 K.

3. Results and discussion

3.1. Microstructural characterization of Er^{3+}, Yb^{3+} co-doped $Y_uGd_wVO_4$ microcrystals.

The normalized intensity XRD patterns of Er^{3+}, Yb^{3+}: $Y_uGd_wVO_4$ MCs synthesized by the solid-state reaction method are displayed in Fig. 1(a). These patterns were compared to standard JCPDS Cards no 017-0260 and 082-1968 of $GdVO_4$ and YVO_4, respectively [47-48]. The observed **XRD** patterns match well with the given standard patterns and their sharp peak indicate the formation of highly crystalline materials in the tetragonal phase with the $I4_1/amd$ space group. This is crucial for the application intended by this work, because higher crystallinity could be explained by less defects and then stronger luminescence features [49]. There was no intermediate or mixed phase observed except slight shifts of all diffraction peaks to the lower angle side with the increase of the Gd^{3+} concentration from 0 to 79 at. % within the Er^{3+}, Yb^{3+}: $Y_uGd_wVO_4$ MCs due to the difference between the ionic radii of Y^{3+} and Gd^{3+} ions [50]. The inset in Fig. 1(a) shows magnifications of the three intense shifted peaks mentioned with stars in Fig. 1(a), corresponding to the (200), (112) and (312) planes. These peak displacements are according to the variation of the unit cell dimensions related to the

change of the ionic size, which can be ultimately related to the ionic radius of Gd^{3+} (1.053 Å) ions that is slightly larger than those of Y^{3+} (1.019 Å), Er^{3+} (1.004 Å) and Yb^{3+} (0.985 Å) ions (coordination number = 8) [50].

To confirm the phase purity and to determine the structural details of the synthesized compounds, Rietveld refinements of the powder diffraction data have been performed using the FullProf program. The peak profile has been defined using the Pseudo-Voigt function. Fig. 1(b), (c), (d) and (e) presents the Rietveld data fit on X-ray diffraction data for the Er^{3+}, Yb^{3+}: $Y_uGd_wVO_4$ MCs with the difference pattern between observed and calculated data. The crystal structural cell and parameters as well as reliability factors (R_p, R_{wp}, and R_{exp}) and goodness of fit (χ^2) for the Er^{3+}, Yb^{3+}: $Y_uGd_wVO_4$ MCs are displayed in Table 1.

The goodness of fit, representing the difference between the weighted and expected profiles, is calculated using the following expression: $\chi^2 = (R_{wp} / R_{exp})^2$, then whenever the ($\chi^2$) will be closer to the unit whenever the fit will be better [51]. In this work, the obtained (χ^2) values for all the refined patterns were found to be lower than the 2.75 value obtained by Muhr et *al.* for the Eu^{3+}: $GdVO_4$ [52]. In fact, these lower values of (χ^2) state the fit accuracy, and the good quality and high precision of the refinement.

The substitution of Y^{3+} ions (r = 1.019 Å) by the Gd^{3+} ions with larger radii (r = 1.053 Å) within the Er^{3+}, Yb^{3+}: $Y_uGd_wVO_4$ compound induces an increase in unit cell parameters with increasing its atomic concentration (see Table 1). In fact, the increase of these *a* and *c* crystallographic parameters of Er^{3+}, Yb^{3+}: $Y_uGd_wVO_4$ results in a host lattice expand. This expansion could be brought on by occupying the interstitial site of host lattice [53]. This replacement of Y^{3+} ions with Gd^{3+} ions caused an increase in cell volumes to be raised from 317.800 $Å^3$ for the Er^{3+}, Yb^{3+}: $Y_{0.79}VO_4$ to 325.856 $Å^3$ for the Er^{3+}, Yb^{3+}: $Gd_{0.79}VO_4$ (see Table 1).

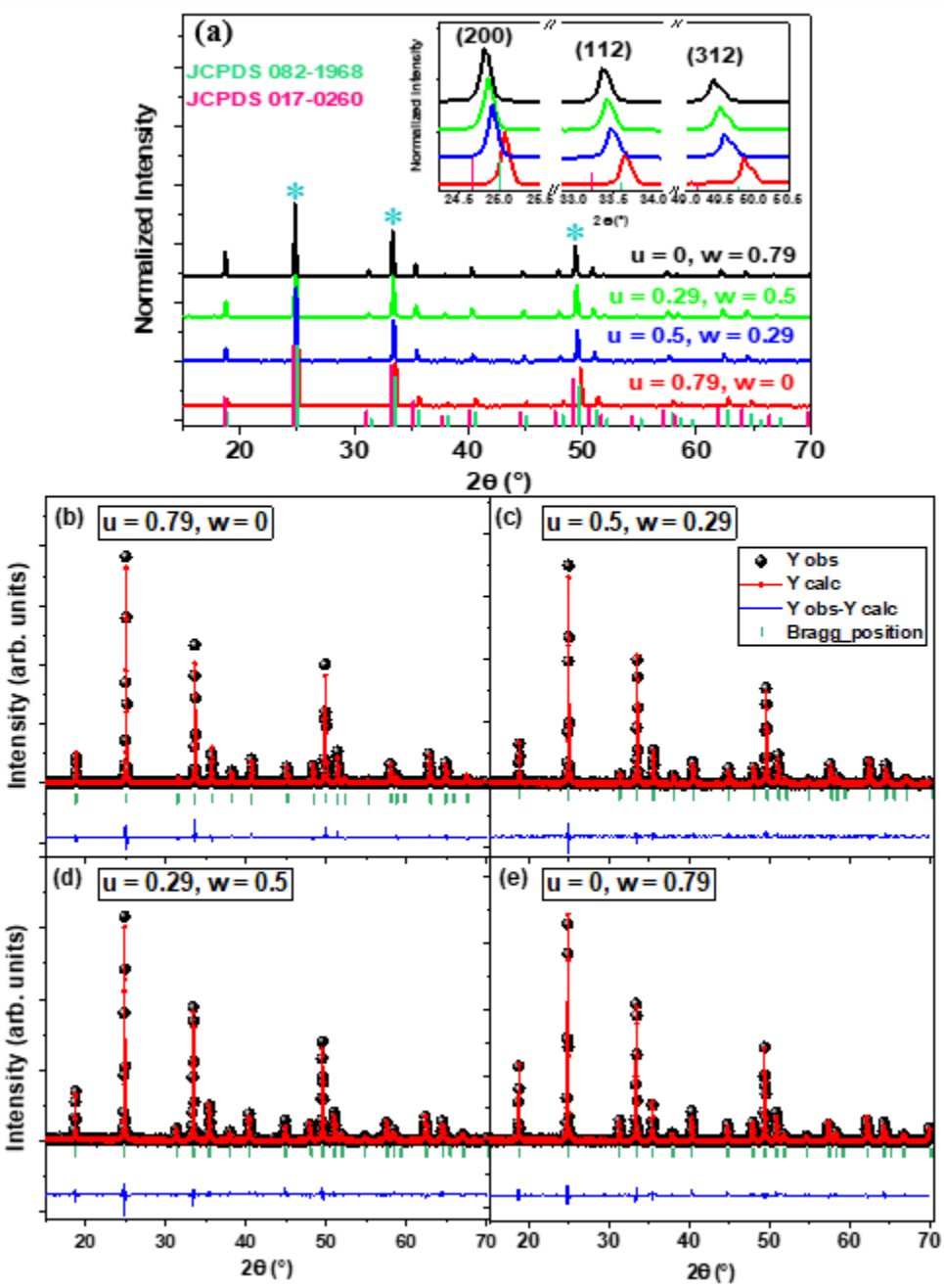

Fig. 1. (a) Normalized intensity X-ray diffraction patterns of Er^{3+}, Yb^{3+}: $Y_uGd_wVO_4$ MCs synthesized by the solid-state reaction method. The standard XRD patterns, corresponding to $GdVO_4$ (JCPDS data, PDF card No. 017-0260) and YVO_4 (JCPDS data, PDF card No. 082-1968) were included for comparison. Inset shows magnifications of the three intense shifted peaks mentioned with stars. (b), (c), (d) and (e) Rietveld refinement for Er^{3+}, Yb^{3+}: $Y_uGd_wVO_4$ MCs: the observed result is represented by black dots, the calculated profile after Rietveld refinement is presented by solid red line and the difference between both of them is presented in the bottom by blue line. The Bragg peak positions are shown above to the difference plot with green bars.

Table 1. Crystal structural parameters of analyzed Er^{3+}, Yb^{3+}: $Y_uGd_wVO_4$ MCs calculated using Rietveld refinement, expressed in the space group $I4_1/amd$ in the tetragonal system.

	Er^{3+}, Yb^{3+}: $Y_{0.79}VO_4$	Er^{3+}, Yb^{3+}: $Y_{0.5}Gd_{0.29}VO_4$	Er^{3+}, Yb^{3+}: $Y_{0.29}Gd_{0.5}VO_4$	Er^{3+}, Yb^{3+}: $Gd_{0.79}VO_4$
***a* = *b* (Å)**	7.111	7.149	7.164	7.177
***c* (Å)**	6.285	6.308	6.318	6.327
c* /*a	0.884	0.882	0.882	0.882
Cell volume (Å^3)	317.800	322.300	324.288	325.856
R_p (%) **R_{wp} (%)** **R_{exp} (%)**	18.7 22.9 16.7	23.7 26.8 24.0	25.7 28.5 24.1	17.9 20.4 16.6
χ^2	1.89	1.24	1.40	1.52

R_p: profile factor.
R_{wp}: R-weighted profile factor.
R_{exp}: R "expected" in the absence of systematic error.

To compare the structural change occurred by introducing Gd^{3+} with the literature, the cell volumes dependent on the atomic concentration of Gd^{3+} ions of the as prepared samples has been plotted in Fig. 2. A relevant comparison with the results obtained by Tyminski *et al.* [54] has been shown also in Fig. 2. It has been found that the cell volumes increases from 306.1 Å^3 to 314.8, 318.8 and 324.5 Å^3, respectively, with the replacement of Lu^{3+} ions (r = 0.977 Å) with La^{3+}, Y^{3+} and Gd^{3+} ions with larger radius of 1.160, 1.019 and 1.053 Å, respectively [54]. A very small difference in volumes could be observed between the 1 Er^{3+}, 20 Yb^{3+}: $Y_{0.79}VO_4$ and 1 Er^{3+}, 20 Yb^{3+}: $Gd_{0.79}VO_4$ samples of this study in comparison with the same samples developed by Tyminski *et al.* [54]. This difference could be attributed to the difference in particle size [37]. Therefore, a larger radii for Ln ion based material host may raise the cell parameters and then the cell volumes.

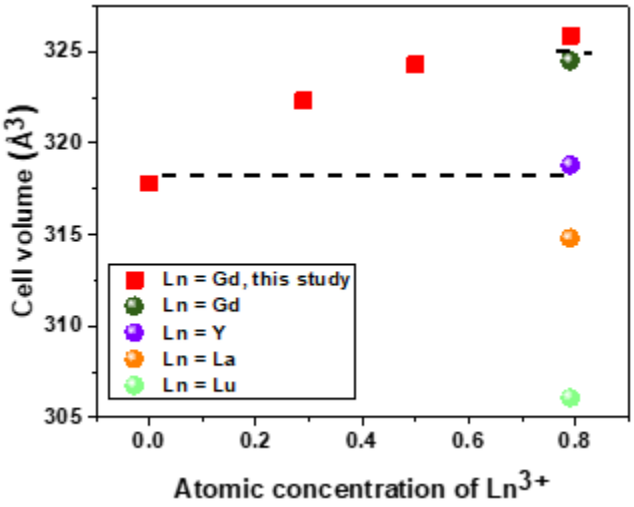

Fig. 2. Stoichiometric effect on the Crystal structural feature of the Er^{3+}, Yb^{3+}: $Y_uGd_wVO_4$ MCs compared to the results obtained by Tyminski *et al.* for the Er^{3+}, Yb^{3+}: $REVO_4$ (RE = Gd, Y, La and Lu). The squares represents the data obtained by the samples of this work. The circles represents the data obtained from the work done by Tyminski *et al.*.

Fig. 3 display typical SEM images of Er^{3+}, Yb^{3+}: $Y_uGd_wVO_4$ MCs. This figure illustrates that all the Er^{3+}, Yb^{3+}: $Y_uGd_wVO_4$ prepared samples presents the same features. Such as those images show grains in the micron range or even larger, that have more or less homogeneous smooth surfaces.

They are clearly discrete from each other where some of them are agglomerated into larger crystals in some regions and they are distributed in a heterogeneous way.

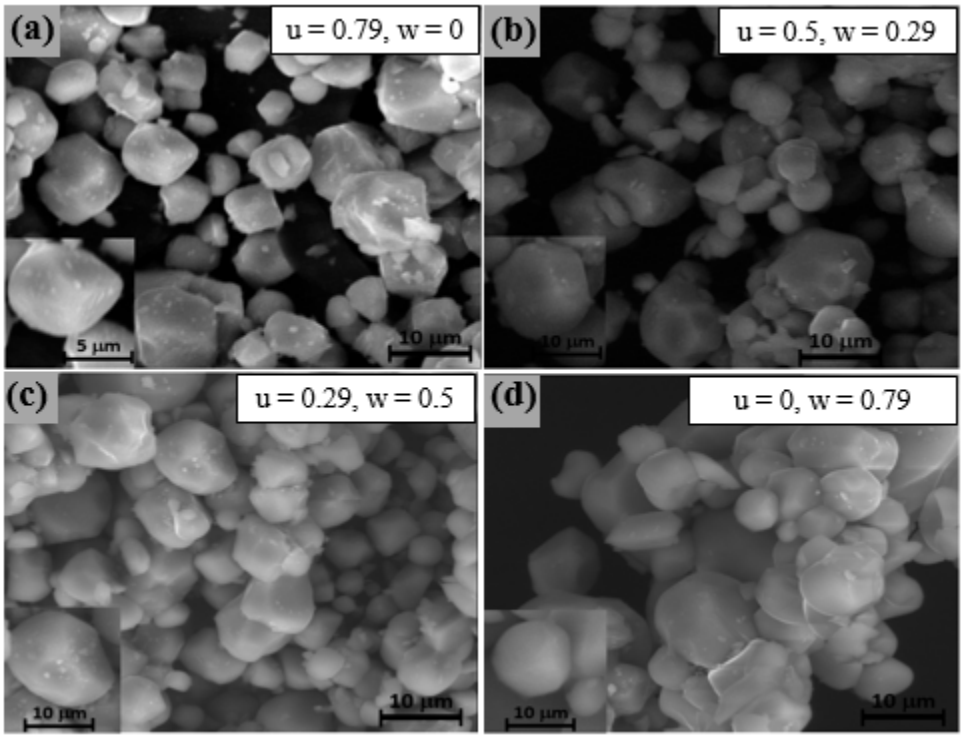

Fig. 3. SEM images of the as obtained Er^{3+}, Yb^{3+}: $Y_uGd_wVO_4$ MCs. u and w being the atomic concentrations of Y^{3+} and Gd^{3+} ions inserted in the co-doped $Y_uGd_wVO_4$ rare earth vanadate host.

Fig. 4(a) shows the FTIR spectra of Er^{3+}, Yb^{3+}: $Y_uGd_wVO_4$ synthesized MCs. No differences exist between the spectra of all the prepared compounds. All the spectra are dominated by two stretching vibration bands attributed to the Gd-O and/ or Y-O bond and to the V-O bond in the VO_4 group of the host lattice [55-57]. The changes of the phonon vibration energies of those observed bands according to the atomic concentration of Gd^{3+} ions are presented in Fig. 4(b).

The phonon vibration energy of the V-O bond varies in the 738-762 cm^{-1} interval from an analyzed rare earth vanadate host to another one, without showing any tendency of variation with the increase of the atomic concentration of Gd^{3+} ions at the expense of Y^{3+} ions. This variation could be related to the anisotropy in the VO_4 coordination. However, the strength of the crystal field in the Gd-O and/ or Y-O bonds seems to be rather constant for all the analyzed samples and they are observed at around 450 cm^{-1} (see Inset of Fig. 4(a), and Fig. 4(b)). It appears also, for all shown spectra in Fig. 4(a), several weak absorption bands extended in the 1465-985 cm^{-1}, 3084-2809 cm^{-1} and 3900-3569 cm^{-1} ranges, which they are attributed to the H-O-H groups of water molecules formed in view of the climate humidity [55]. The vibration energy of these bands doesn't change with the variation of the atomic concentration of Y^{3+} and Gd^{3+} ions inserted in the studied rare earth vanadate host.

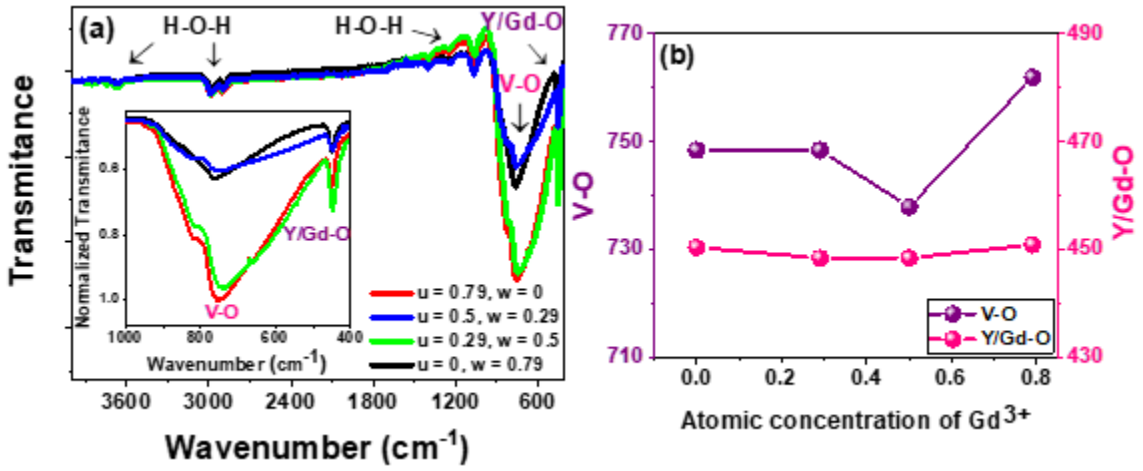

Fig. 4. (a) FTIR spectra of Er^{3+}, Yb^{3+}: $Y_uGd_wVO_4$ MCs obtained by the solid-state synthesis method. Inset shows magnifications of the normalized transmittance of the Gd-O and/or Y-O and the V-O absorption bands. (b) Dependence of the phonon vibration energies of V-O and Y/Gd-O bonds on the atomic concentration of Gd^{3+} ions in the Er^{3+}, Yb^{3+}: $Y_uGd_wVO_4$ rare earth vanadate host.

3.2. Dependence of the luminescent anti-Stokes emission of Er^{3+}, Yb^{3+}: $Y_uGd_wVO_4$ MCs with the excitation laser power density and the stoichiometry.

The room temperature photoluminescence anti-Stokes emission spectra in the 500-580 nm spectral range of the Er^{3+}, Yb^{3+}: $Y_uGd_wVO_4$ MCs excited at 980 nm were recorded at different pumping power densities in the range of 20-445 W cm^{-2} as shown in Fig. 5.

All these spectra exhibits two strong emission bands located in the green visible region, which comes from the $^2H_{11/2}\rightarrow{}^4I_{15/2}$ (~525 nm) and $^4S_{3/2}\rightarrow{}^4I_{15/2}$ (~552 nm) electronic transitions of Er^{3+} ions [58]. Even at low laser excitation power density (20 W cm^{-2}), the green anti-Stokes luminescence of all the analyzed samples can be observed and its intensity increases continuously as the excitation power density increases which can be correlated to the increasing electronic populations in the excited states of the doping ions (see Fig. 5). Nevertheless, the one coming from the $^4S_{3/2}\rightarrow{}^4I_{15/2}$ transition doesn't increase anymore only from the following excitation power density values: 389, 417 and 361 W cm^{-2}, respectively, for the Er^{3+}, Yb^{3+}: $Y_{0.79}VO_4$; Er^{3+}, Yb^{3+}: $Y_{0.29}Gd_{0.5}VO_4$ and Er^{3+}, Yb^{3+}: $Gd_{0.79}VO_4$ compounds and starts to decrease gradually with increasing the excitation power density (see Fig. 5(a), (c) and (d)). At low pump power densities, the intensity of green emission band coming from the $^4S_{3/2}\rightarrow{}^4I_{15/2}$ transition is more intense than that coming from the $^2H_{11/2}\rightarrow{}^4I_{15/2}$ transition for all the prepared compounds. However, from the pump power density value of 87 W cm^{-2}, the emission intensity coming from the $^2H_{11/2}\rightarrow{}^4I_{15/2}$ transition becomes more intense than that coming from the $^4S_{3/2}\rightarrow{}^4I_{15/2}$ transition for the Er^{3+}, Yb^{3+}: $Y_{0.79}VO_4$ and Er^{3+}, Yb^{3+}: $Y_{0.5}Gd_{0.29}VO_4$ compounds (see Fig. 5(a) and (b)). Whereas, for the Er^{3+}, Yb^{3+}: $Y_{0.29}Gd_{0.5}VO_4$ and Er^{3+}, Yb^{3+}: $Gd_{0.79}VO_4$ compounds, this inversion has been seen from the pump power density value of 119 W cm^{-2} (see Fig. 5(c) and (d)).

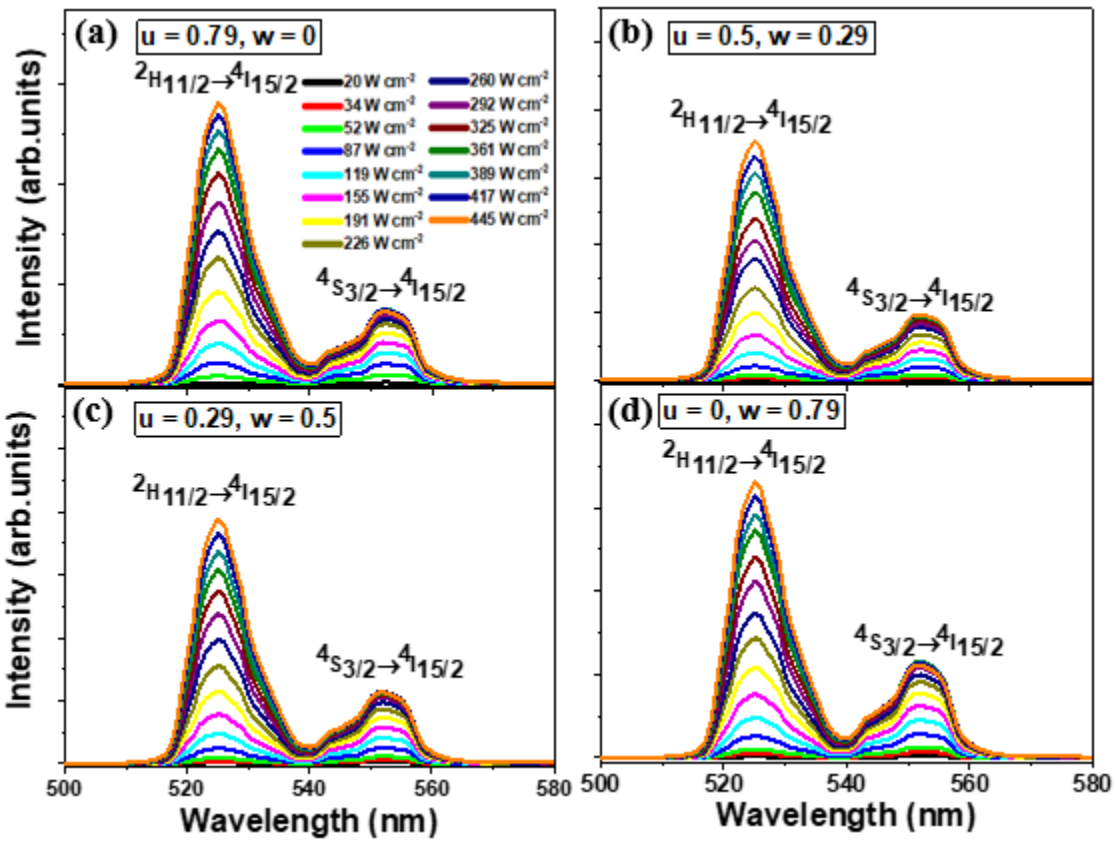

Fig. 5. Excitation laser power density dependent room temperature anti-Stokes emission spectra for Er^{3+}, Yb^{3+}: $Y_uGd_wVO_4$ MCs excited with a diode laser emitting at 980 nm using different pump power densities (20-445 W cm^{-2}) and recorded in the 500-580 nm range. u and w being, respectively, the atomic concentrations of Y^{3+} and Gd^{3+} ions inserted in the rare earth vanadate host.

As mentioned by Li *et al.* [59] in their work that for a non-saturated anti-Stokes process, the anti-Stokes emission intensity (I_{up}) is proportional to the excitation laser power (P), i.e., $I_{up} \propto P^n$, where n is the number of NIR photons involved in the process to populate the upper emitting level. Then, to determine the excitation power density range in which we should work without saturating the anti-Stokes emission intensities for all the Er^{3+}, Yb^{3+}: $Y_uGd_wVO_4$ prepared compounds, the double logarithmic power density dependence of the integrated intensity of the two green observed emissions was plotted as shown in Fig. 6. The linear behavior follows by the experimental data of the green integrated intensity emissions can be extended to around a laser excitation power density of 226 W cm^{-2} in all the samples and set-up used. Therefore, the required photons number for populating the $^2H_{11/2}$ and $^4S_{3/2}$ levels can be easily determined from the linear extrapolation slope of the experimental data shown in Fig. 6. With a slope value around 2, these emissions are mainly two-photon anti-Stokes process. However, at higher excitation power densities, above 226 W cm^{-2}, the experimental data of these green integrated emission intensities doesn't follow anymore a linear tendency with the excitation power densities. Above this value, the saturation regime is reached and we can mention that there are two excitation regimes that characterize the excitation power density region of this study.

Below 226 W cm^{-2}, the ratio of slopes for both emissions generated from the $^2H_{11/2}$ and $^4S_{3/2}$ levels, n_H and n_S, respectively, decrease slightly from 1.32 to 1.23 with increasing the Gd^{3+} atomic concentration from 0 to 79 at. % within the Er^{3+}, Yb^{3+}: $Y_uGd_wVO_4$ MCs. This decreasing may reflect the dependence of the emitting level populations with the host materials, and then as much as the concentration of Gd^{3+} ions is present in the studied materials as much as the $^2H_{11/2}$ upper emitting level will be populated. Therefore, the increasing of Gd^{3+} ion concentration may induce lower non-radiative desecxitation and then higher thermometric performance [49].

As minutely discussed previously in the work done by Marciniak *et al.* [40], in where it was well highlighted that the luminescence thermal behavior of luminescent thermometers will depend largely on the excitation power density used and then to reach high sensitivity, the materials should be excited in the non-saturation regime. Thus, the luminescence thermometric characterization of the samples can be performed under anti-Stokes process with any excitation power density lower than 226 W cm^{-2} without saturating the anti-Stokes emission intensities. It should be mentioned here that the inversion of the emission intensities generated by the two levels $^2H_{11/2}$ and $^4S_{3/2}$ at low excitation power densities not exceeding 226 W cm^{-2}, is not necessarily due to a saturation process (see Fig. 5). But it is related especially to a sample heating phenomenon generated by higher excitation power densities.

It is well known that the UC processes are very sensitive to the crystal field of the host matrix [43]. In the present study, the crystal field effect created by the host material surrounding the Er^{3+} ion substitute Y and/or Gd sites in the lattice allow to the $^2H_{11/2}$ and $^4S_{3/2}$ energy levels of Er^{3+} ion to be split into different energy Stark sublevels depending on the site symmetry and the strength of the crystal field. As the strength of the crystal field increases, the splitting of energy sublevels becomes greater. And the energy gap between the $^2H_{11/2}$ and $^4S_{3/2}$ levels becomes smaller, then the population of the $^2H_{11/2}$ states becomes more important as the temperature increases, and the level becomes more populated. This results in the energy level populations increases with the strength of the crystal field. Indeed, one of the most promising effects concerning the improvement of energy level population can be achieved by the modification of the activation energy of the thermal quenching process via the modulation of the relative position of excited and ground states via the modification of crystal field strength [60]. Based on the above understanding, the dominant effect in the behavior of the studied samples may occur due to the electronic population distribution observed in Fig. 6 more than to the change of the crystal field distribution discussed in *Section 3.1*, which is related to the unit cell.

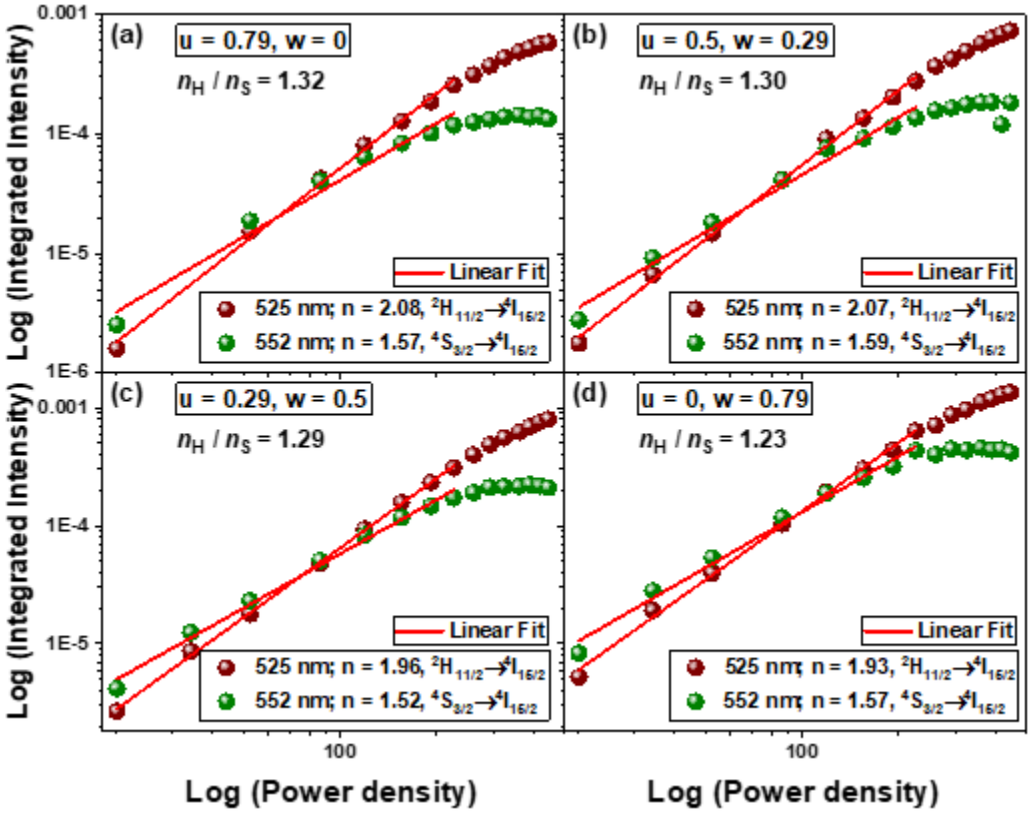

Fig. 6. Measured integrated intensities of the green emission bands versus pump power density, after excitation at 980 nm; linear fittings correspond to the equation $I_{up} \propto P^n$, and n_H and n_S corresponds

to the slopes for the two $^2H_{11/2}$ and $^4S_{3/2}$ levels, respectively. u and w being, respectively, the atomic concentrations of Y^{3+} and Gd^{3+} ions inserted in the Er^{3+}, Yb^{3+}: $Y_uGd_wVO_4$ rare earth vanadate host.

3.3. Experimental luminescence temperature-sensing performance of Er^{3+}, Yb^{3+}: $Y_uGd_wVO_4$ MCs under anti-Stokes processes determined using OriginLab@software.

The ratio of the emission intensities of two distinct transitions from the same emitting center provides a robust temperature measurement approach. Using the Er^{3+} green emissions to obtain this ratio, the FIR from them can be described as follows [9,14]:

$$FIR = \frac{I_H}{I_S} = \frac{g_H \vartheta_H A_H}{g_S \vartheta_S A_S} exp\left(-\frac{\Delta E}{k_B T}\right) = Bexp\left(-\frac{\Delta E}{k_B T}\right) \quad (1)$$

being I_H and I_S, the integrated intensity of the two green emissions arising from the $^2H_{11/2}$ and $^4S_{3/2}$ emitting levels, respectively, from Er^{3+} ions; g_H and g_S are the degeneracy of the $^2H_{11/2}$ and $^4S_{3/2}$ levels, respectively; ν_H, ν_S, A_H and A_S are the frequencies and spontaneous emission rates corresponding to these levels; ΔE is the energy gap between the $^2H_{11/2}$ and $^4S_{3/2}$ levels in the particular hosts ($Y_uGd_wVO_4$ in that case); k_B is the Boltzmann's constant; T is the absolute temperature and B is the pre-exponential constant.

To evaluate the temperature sensing performances of different thermometers, it is vital to quantify the thermal sensitivity, S, of the fluorescence intensity ratio. Such as for a single emitting center, it can be defined in absolute terms, or absolute sensitivity S_a [9]:

$$S_a = \frac{\partial FIR}{\partial T} = FIR\frac{\Delta E}{k_B T^2} \quad (2)$$

And in relative terms as it is known by relative thermal sensitivity [9]:

$$S_r = 100\% * \left|\frac{1}{FIR}\frac{\partial FIR}{\partial T}\right| = 100\% * \frac{\Delta E}{k_B T^2} \quad (3)$$

Also, the uncertainty in temperature is a significant factor for judging a temperature sensor, and it can be estimated from the sensitivity of the detection system and the calculated relative thermal sensitivity, according to the following equation [61]:

$$\delta T = \frac{1}{S_r}\frac{\delta FIR}{FIR} \quad (4)$$

where $\partial FIR/FIR$ is the sensitivity of the detection system, with a value, in our case of 0.5 % [62].

As discussed in the last section, to determine the heating effect generated by the excitation power density on the thermometric performances according to the atomic concentrations of Y^{3+} and Gd^{3+} ions inserted in the Er^{3+}, Yb^{3+}: $Y_uGd_wVO_4$ rare earth vanadate hosts, we will excite in the non-saturated regime with pump power densities less than 226 W cm^{-2}. Consequently, we decided to excite with 20 and 155 W cm^{-2} of pump power densities.

To evaluate the actual temperature sensing capabilities of the Er^{3+}, Yb^{3+}: $Y_uGd_wVO_4$ developed sensors operated under anti-Stokes condition and to analyze the effect of the excitation laser power density values as well as the impact of the atomic concentration of Y^{3+} and Gd^{3+} ions inserted in the studied rare earth vanadate hosts on them, the dependence of their temperature anti-Stokes emission spectra obtained under 980 nm diode laser excitation was measured at two different excitation laser power densities of 20 and 155 W cm^{-2} in the 303 to 513 K temperature range and in the 510-570 nm spectral range (see Fig. 7).

All the spectra show two green emission bands corresponding to $^2H_{11/2} \rightarrow {}^4I_{15/2}$ (~525 nm) and $^4S_{3/2} \rightarrow {}^4I_{15/2}$ (~553 nm) transitions of Er^{3+} ions [58]. At low excitation power density of 20 W cm^{-2} and at low temperatures, the emission intensity coming from the $^4S_{3/2}$ level is more intense than that coming from the $^2H_{11/2}$ level for all the analyzed samples (see Fig. 7(a), (c), (e) and (g)). With increasing temperature, a thermal agitation leads the $^2H_{11/2}$ level to be populated at expenses of the

$^4S_{3/2}$ level and when the temperature is sufficiently high, the emission intensity coming from it becomes stronger than that coming from the $^4S_{3/2}$ level (see Fig. 7(a), (c), (e) and (g)). However, at higher excitation power density of 155 W cm^{-2}, even at low temperatures reaching 303 K, the emission arising from the $^4S_{3/2}$ manifold appears weaker than that arising from the $^2H_{11/2}$ manifold for all the analyzed samples (see Fig. 7(b), (d), (f), and (h)). Then, we can judge that there is an extra-heating of the samples generated by the pumping power density, which may represent the origin of the inversion of the emission intensities of the $^2H_{11/2}$ and $^4S_{3/2}$ levels when we kept the same low temperature and we increased the pump power density to 155 W cm^{-2} of value (see Fig. 7). Taking into account the discussion given by Marciniak *et al.* [40], as a consequence, a decrease of the thermometric performance should be observed.

The experimental energy gap $\Delta E`$ can be deduced by fitting the experimental PL spectrum recorded at RT and calculating the energy separation between the barycenters of the $^2H_{11/2}$ and $^4S_{3/2}$ levels. The obtained values of $\Delta E`$ for all the prepared MCs excited at 20 and 155 W cm^{-2} are summarized in Table 2. As expected, all the obtained values are very similar due to the shielding of the lanthanide ion 4f electrons in relation of the crystal field and fall in the 880-901 cm^{-1} range. A small increase in the excitation power density from 20 to 155 W cm^{-2} does not affect the value of the energy gap and it remains almost the same for all studied compounds.

For the Er^{3+}, Yb^{3+}: $Y_uGd_wVO_4$ studied samples, increasing the concentration of Gd^{3+} ions at the expense of the Y^{3+} ions with lower ionic size may induce a lattice expansion that can be illustrated in the decreasing of the lattice field surrounding the sensitive Er^{3+} ions. Then the $\Delta E`$ value representing the energy difference between the two TCLs of Er^{3+} ions inserted in the $Y_uGd_wVO_4$ host will be decreased from a sample to another one with higher atomic concentration of Gd^{3+} ions, as well highlighted in Table 2. This reflects that whenever the atomic concentration of Gd^{3+} ions is higher whenever the effect of the crystal field is less important and the distance between the sites occupied by the Er^{3+} ions is larger. Consequently, the distortion of the site occupied by the Er^{3+} ions will be lower as much as the concentration of Gd^{3+} ions will be increased.

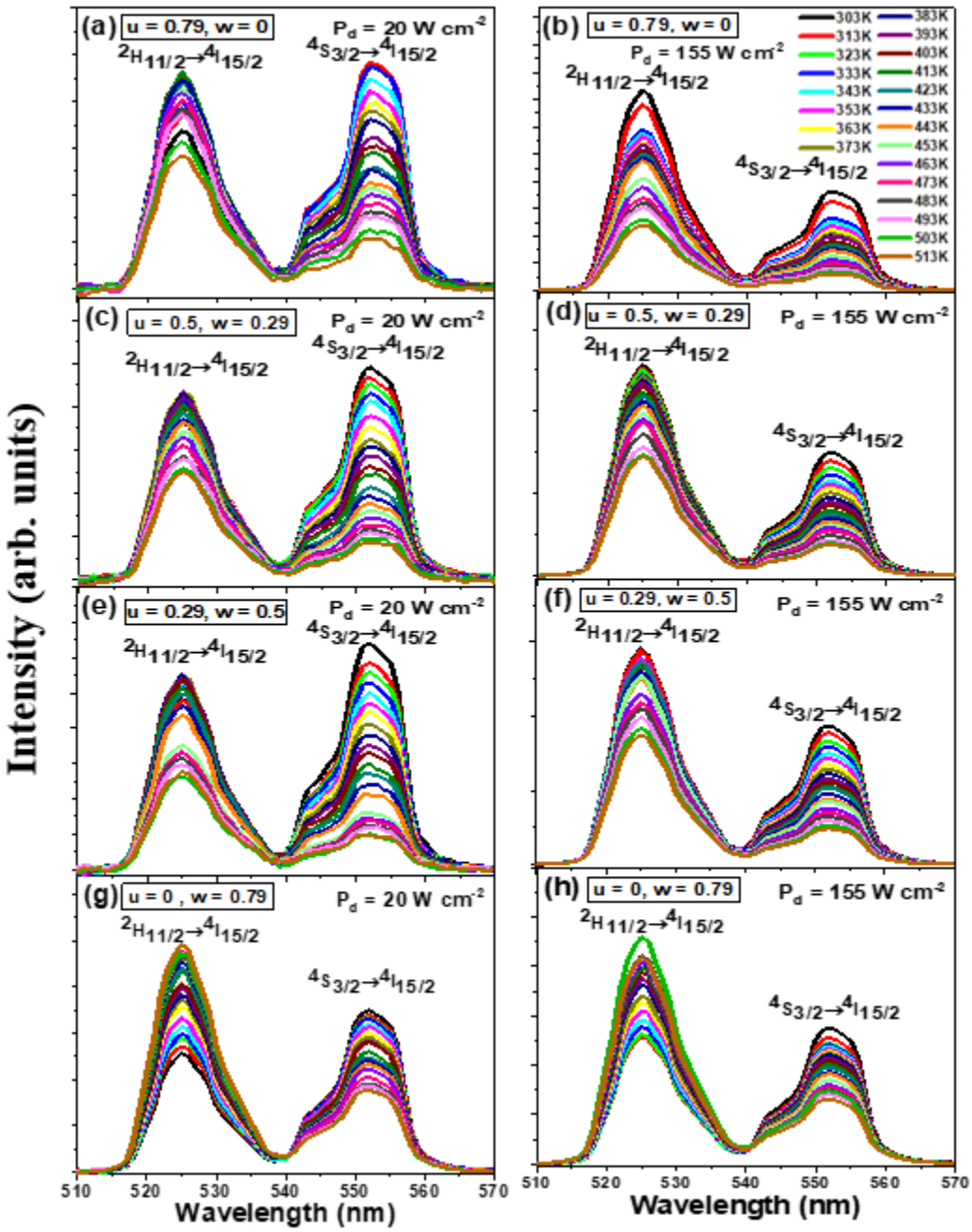

Fig. 7. Temperature dependent anti-Stokes emission spectra of Er^{3+}, Yb^{3+}: $Y_uGd_wVO_4$ MCs measured in the 303-513 K temperature range and excited with 980 nm laser diode at two different excitation laser power densities of 20 and 155 W cm^{-2}. u and w being, respectively, the atomic concentrations of Y^{3+} and Gd^{3+} ions inserted in the rare earth vanadate host.

3.3.1. Thermometric ratio dependent on the excitation laser power density and the stoichiometry.

Using the experimental spectra shown in Fig. 7, and using the integral area of each manifold, the FIR ratio of $^2H_{11/2}\rightarrow{}^4I_{15/2}$ versus $^4S_{3/2}\rightarrow{}^4I_{15/2}$, as expressed in equation (1), has been calculated for each temperature and each excitation laser power density used. The evolution of the FIR with temperature together with the fitting curves using equation (1) for the Er^{3+}, Yb^{3+}: $Y_uGd_wVO_4$ MCs

operated under anti-Stokes condition with pumping at two different excitation power densities (20 and 155 W cm^{-2}) are depicted in Fig. 8(a).

Whatever the atomic concentration of Y^{3+} and Gd^{3+} ions in the rare earth vanadate host and whatever the excitation power density used, the FIR values increase monotonously as the temperature increases following an exponential dependence for all the studied samples in the 303-513 K temperature range (see Fig. 8(a)). This behavior follows strictly the Boltzmann distribution law and then we are not working in the saturation range [40]. Since the saturation regime is reached only from the value of 226 W cm^{-2}, then this behavior confirms well that the emission intensity inversion between the $^2H_{11/2}$ and $^4S_{3/2}$ level emissions at RT, seen earlier for the excitation power density of 155 W cm^{-2} (in Fig. 7), is not related to a saturation phenomenon but it is related only to a heating effect generated by the high excitation power density.

In the 303-513 K temperature range, the FIR values obtained at an excitation power density of 20 W cm^{-2} always remain lower than those obtained at an excitation power density of 155 W cm^{-2} for all the studied samples (see Fig. 8(a)). At low excitation power density of 20 W cm^{-2}, the representative FIR curves are almost overlapped for all the Er^{3+}, Yb^{3+}: $Y_uGd_wVO_4$ studied samples. Then, at each given temperature, the FIR values are rather the same value whatever the atomic concentration of Y^{3+} and Gd^{3+} ions. However, at higher excitation power density of 155 W cm^{-2}, it appears a large difference between the FIR values at each given temperature, such as the increase of the Gd atomic concentration within the Er^{3+}, Yb^{3+}: $Y_uGd_wVO_4$ MCs lead to the decreasing of these values (see Fig. 8(a)). Then, it can be deduced that as lower as the Gd atomic concentration used as much as the population of the $^2H_{11/2}$ level at the expense of the $^4S_{3/2}$ level will be promoted in view of the crystal field effect which is most important in the Er^{3+}, Yb^{3+}: $Y_uGd_wVO_4$ MCs with higher atomic concentration of Y^{3+} ions.
The equation (1) describing the Boltzmann distribution law can be rewritten in a logarithm form as:

$$\ln(FIR) = \ln(B) + \left(\frac{-\Delta E}{k_B T}\right) = \ln(B) + \left(-\frac{C}{T}\right) \qquad (5)$$

where *B* and *C* are the constants that are needed to be determined in the experimental calibration of our sensors.

The logarithm plot of the FIR values as a function of the reciprocal absolute temperature in the 303-513 K range for the Er^{3+}, Yb^{3+}: $Y_uGd_wVO_4$ samples operated under anti-Stokes condition and at two different excitation power densities of 20 and 155 W cm^{-2} are shown in Fig. 8(b).

The experimental data for all the studied samples follow the expected linear tendency that can well be fitted to a straight line according to equation (5). They show a good correlation between experiments and theory (see Fig. 8(b)), knowing that all the experimental data and the theoretical ones exhibit a regression factor over 99 %. With exciting at 20 W cm^{-2} pump power density, the experimental data obtained for the Er^{3+}, Yb^{3+}: $Y_uGd_wVO_4$ compounds are approximately overlapped and presents almost the same angle of inclination, then they should provide same slope and intersection values. However, with exciting at 155 W cm^{-2} pump power density, they are little apart from each other and they became more inclined with moving from lower atomic concentration of Gd^{3+} ions to higher ones. Subsequently, it may result in an increasing in the slope values with the increase of the concentration of Gd^{3+} ions and different intersection values will be obtained for all the analyzed samples.

The fitted energy gap value (slope at a nearby factor, k_B), ΔE_{FIR}, as well as the pre-exponential factor (intersection), B_{FIR}, for the different samples excited at the two different pump power densities can be derived easily from the fitting of the ln (FIR) data and they are listed in Table 2. Following the same line of reasoning, the ΔE_{FIR} and the B_{FIR} values should be the same for all the studied compounds excited at 20 W cm^{-2}. While, for a pump power density of 155 W cm^{-2}, they should be different such as the ΔE_{FIR} values will be increased with the increase of the concentration of Gd^{3+} ions within the Er^{3+}, Yb^{3+}: $Y_uGd_wVO_4$ MCs.

The results shown in Table 2 confirms well that the obtained ΔE_{FIR} and B_{FIR} values are nearly the same for all the studied compounds excited at low excitation power density of 20 W cm^{-2}, and

they were found to be in the ranges 736-770 cm^{-1} and 22.5-25.6, respectively. However, they are widely different with exciting at 155 W cm^{-2} and their values vary in the ranges 419-725 cm^{-1} and 14-26.2, respectively. Also, at this later excitation power density, these parameters show a progressive rise in their values whenever the atomic concentration of Gd^{3+} ions within the Er^{3+}, Yb^{3+}: $Y_uGd_wVO_4$ MCs increases, which may result in the increase of the thermometric performances of the analyzed thermometers.

It is obviously seen that for all the studied Er^{3+}, Yb^{3+}: $Y_uGd_wVO_4$ compounds the ΔE_{FIR} values determined at low pump power density (20 W cm^{-2}) always remain greater than those determined at higher pump power density (155 W cm^{-2}), such as for both cases (low and high pump power densities) they underestimate the experimental energy gap value $\Delta E`$. Therefore, it will be an advance to conclude that whenever the $\Delta E_{FIR}$ value is lower than the experimental one $\Delta E`$, whenever the sample will be more heated. As has been illustrated [28,46], the thermometric parameters will be affected by these heating effects and then, they will be less efficient.

In fact, equation (1) is strictly right when the electronic population between the two TCLs is strictly governed by Boltzmann distribution law. However, as mentioned in the introduction, several factors will impact the real luminescence intensity ratio, and then the actual thermal sensitivity [22,44-45]. As reported by Li *et al.* [44], the δE (%) data; representing the difference percentage of the fitted ΔE_{FIR} energy gap from the $\Delta E`$ expected one which is calculated using the multi-peak fitting structure of the emission spectrum recorded at 303 K; calculated according to the following formula: $\delta E = (\Delta E` - \Delta E_{FIR})$ x 100/ $\Delta E`$, can be correlated with the increase of importance of the thermal quenching processes, which will alter the electronic population between the two TCLs making it to differ from Boltzmann distribution law. So, as reported in Table 2, the sample in which the thermal behavior differs less from Boltzmann distribution is the one excited at 980 nm with a pump power density of 20 W cm^{-2}, Er^{3+}, Yb^{3+}: $Gd_{0.79}VO_4$. Then, this sample should have the best relative thermal sensitivity, which will be verified later in the following section.

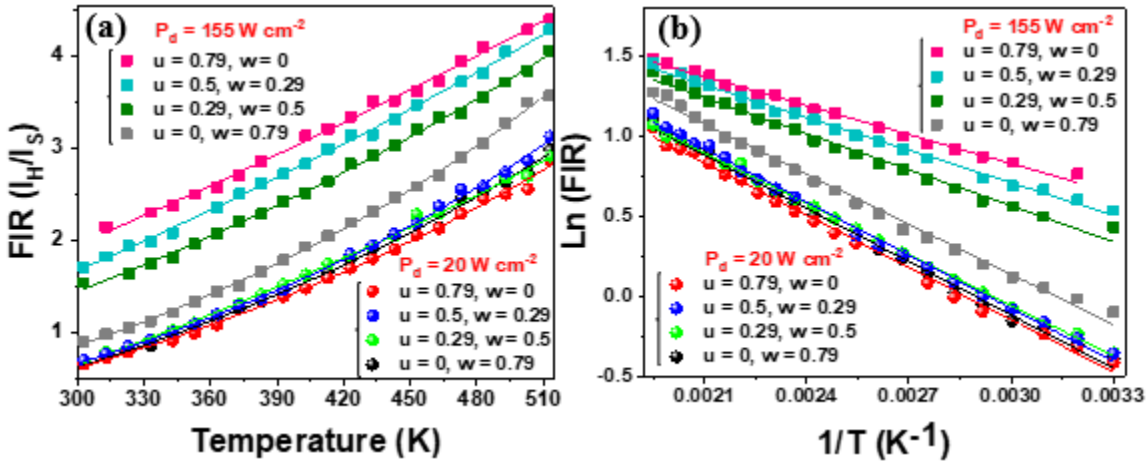

Fig. 8. (a) Integrated fluorescence intensity ratio of the Er^{3+} green anti-Stokes emissions for the I_H/I_S transitions, for the Er^{3+}, Yb^{3+}: $Y_uGd_wVO_4$ MCs excited at two different excitation power densities of 20 and 155 W cm^{-2}, measured in the 303-513 K temperature range. (b) Monolog plot of FIR for Er^{3+}, Yb^{3+}: $Y_uGd_wVO_4$ MCs excited at two different excitation power densities (20 and 155 W cm^{-2}) as a function of the inverse of temperature and the corresponding fitting according to the Boltzmann distribution law described in its logarithm form ($\mathbf{ln}(\boldsymbol{FIR}) = \mathbf{ln}(\boldsymbol{B}) + (\frac{-\Delta \boldsymbol{E}}{\boldsymbol{k_B T}})$).

Table 2. Comparison between the experimental fitted energy gap values and the numerical ones between the $^2H_{11/2}$ and $^4S_{3/2}$ thermalized levels of Er^{3+} ions ($\Delta E`$ fitted from the PL spectra measured at RT, $\Delta E_{FIR}$ fitted from the FIR curves, $\delta E$ is evaluated by $(\Delta E` - \Delta E_{FIR})$ x 100/ $\Delta E`$ and ΔE^{TS} determined using the TeSen Calculator program) and between the pre-exponential constant (B_{FIR} determined from the fitted FIR curves and a determined using the TeSen Calculator program) for the

as-grown Er^{3+}, Yb^{3+}: $Y_uGd_wVO_4$ samples operated under anti-Stokes condition at two different excitation power densities of 20 and 155 W cm^{-2} in the 300-513 K temperature range.

Samples	Power density (W cm^{-2})	ΔE (cm^{-1})	ΔE_{FIR} (cm^{-1})	δE (%)	ΔE^{TS} (cm^{-1})	B_{FIR}	a
Er^{3+}, Yb^{3+}: $Y_{0.79}VO_4$	20	901	755	16	804	22.5	26.7
	155	899	419	53	476	14	18.1
Er^{3+}, Yb^{3+}: $Y_{0.5}Gd_{0.29}VO_4$	20	891	769	14	800	25.6	28.9
	155	890	471	47	508	15.5	18.6
Er^{3+}, Yb^{3+}: $Y_{0.29}Gd_{0.5}VO_4$	20	888	736	17	777	22.6	27.1
	155	889	521	41	541	16.7	18.7
Er^{3+}, Yb^{3+}: $Gd_{0.79}VO_4$	20	884	770	13	767	24.7	24.6
	155	880	725	18	763	26.2	30.9

3.3.2. Laser heating and stoichiometric effects on the thermometric performances.

Using the FIR data and the ΔE_{FIR} values obtained from the linear fit of the logarithm plot of FIR as a function of the reciprocal absolute temperature shown in Fig. 8(b); and with applying the equations (2) and (3), the experimental absolute (S_a) and relative (S_r) thermal sensitivities for all the analyzed samples have been calculated in the 303-513 K temperature range and at the two different excitation power densities of 20 and 155 W cm^{-2} (see Fig. 9). Their optimal values are given in Table 3.

The S_a values for all the studied samples excited at 20 and 155 W cm^{-2} are found to be in the 7.524 x 10^{-3} K^{-1} (303 K) and 14.373 x 10^{-3} K^{-1} (513 K) interval, respectively, for Er^{3+}, Yb^{3+}: $Y_{0.79}VO_4$ excited at 20 W cm^{-2} and for Er^{3+}, Yb^{3+}: $Gd_{0.79}VO_4$ excited at 155 W cm^{-2}. While, for the same excitation power densities of 20 and 155 W cm^{-2}, the S_r values are found to be in the 0.229 % K^{-1} (513 K)- 1.207 % K^{-1} (303 K) interval, respectively, for Er^{3+}, Yb^{3+}: $Y_{0.79}VO_4$ excited at 155 W cm^{-2} and for Er^{3+}, Yb^{3+}: $Gd_{0.79}VO_4$ excited at 20 W cm^{-2} (see Fig. 9).

Fig. 9(a) shows that the S_a values doesn't follow a clear tendency either as a function of temperature or as a function of excitation power density regarded to the atomic concentration of Y^{3+} and Gd^{3+} ions used in the analyzed samples based on Er^{3+}, Yb^{3+}: $Y_uGd_wVO_4$. However, we can assimilate that at low laser excitation power density (20 W cm^{-2}), S_a increases monotonously with temperature without showing a significant difference between their values from a sample to another one with higher or lower atomic concentration of Gd^{3+} ions. Nevertheless, at higher laser excitation power density (155 W cm^{-2}) it is rather stable with temperature for all the analyzed samples, except that for the Er^{3+}, Yb^{3+}: $Gd_{0.79}VO_4$ compound which has the same tendency of variation (increases with temperature) as at low excitation power density (20 W cm^{-2}). In addition, the S_a values obtained for the developed sensors excited at 20 W cm^{-2} always remain lower than those excited at 155 W cm^{-2} up to the temperature of 413 K. From the later temperature, the S_a values of some of them excited at 20 W cm^{-2} becomes higher than those of some sensors excited at 155 W cm^{-2}. It is obviously seen that in the 303-343 K temperature range, the best absolute thermal sensitivity was appreciated by the Er^{3+}, Yb^{3+}: $Y_{0.79}VO_4$ compound excited at 155 W cm^{-2} with a value of 12.901 x 10^{-3} K^{-1} at 313 K. While, in the 343-388 K temperature range, the best one was achieved by the Er^{3+}, Yb^{3+}: $Y_{0.5}Gd_{0.29}VO_4$ compound excited at 155 W cm^{-2} with a value of 12.342 x 10^{-3} K^{-1} at 343 K. At temperatures higher than 388 K, the best one was achieved by the Er^{3+}, Yb^{3+}: $Gd_{0.79}VO_4$ compound excited at 155 W cm^{-2} with a value of 14.373 x 10^{-3} K^{-1} at 513 K.

Regarding to the results presented in Table 3, the optimal S_a values are roughly the same whatever the atomic concentration of Gd^{3+} ions and the excitation laser power density used. They vary in the 11.621-14.373 x 10^{-3} K^{-1} (at 513 K) range and they are found at higher temperature of study for lower excitation power density of 20 W cm^{-2} and at lower one for higher excitation power density of 155 W cm^{-2}. Except, the Er^{3+}, Yb^{3+}: $Gd_{0.79}VO_4$ compound excited at 155 W cm^{-2} has achieved the best absolute sensitivity at a temperature of 513 K.

Taking into account the expression of S_r (equation (3)) which is directly related to the energy gap value multiplied by a nearby factor ($1/(k_B \times T^2)$) and what has already been mentioned above

concerning the ΔE_{FIR} value (from Fig. 8(b)), it is expected that the S_r values will be almost the same at low excitation power density for all the studied compounds and that will not be the same at higher excitation power density. Also, the S_r values determined at low pump power density (20 W cm^{-2}) will always remain greater than those determined at higher pump power density (155 W cm^{-2}). Fig. 9(b) confirms well what is already mentioned above, such as the S_r values decreases gradually as the temperature increases for all the thermal sensors operated at the two different excitation power densities (20 and 155 W cm^{-2}). At an excitation power density of 20 W cm^{-2} and for each given temperature, the S_r values are almost the same for all the analyzed sensors. Whereas for 155 W cm^{-2} excitation power density, they are widely different all along the 303–5013 K temperature range. Then, at low excitation power density of 20 W cm^{-2}, the increase of the atomic concentration of Gd^{3+} ions at the expense of Y^{3+} ions don't affect the S_r of the studied sensors, which is not the same case for higher excitation power density (155 W cm^{-2}). Such as, for the excitation power density of 155 W cm^{-2}, at each given temperature the S_r value rise from a sample to another one with higher atomic concentration of Gd^{3+} ions used. Therefore, for our studied sensors, we may conclude that at higher excitation power density (155 W cm^{-2}) when comparing the relative sensitivity among different hosts, the lattice field surrounding the sensitive Er^{3+} ions will gain an effective importance, which could not be considerable at too low pump power density of excitation (20 W cm^{-2}). In fact, at higher pump power density, as much as the distance between the sites occupied by the sensitive Er^{3+} ions is larger as much as the effect of the crystal field is less important leading to an efficient increase of the relative sensitivity of the temperature sensor. In addition, the S_r values determined at 20 W cm^{-2} always remain higher than those determined at 155 W cm^{-2} along the 303-513 K temperature range of study. Meanwhile, the Er^{3+}, Yb^{3+}: $Gd_{0.79}VO_4$ excited at 155 W cm^{-2} presents S_r values that are nearly equal to those of analyzed samples excited at a lower excitation power density of 20 W cm^{-2}. Then, we could mention that the later sample excited at 155 W cm^{-2} with the higher concentration of Gd^{3+} ions could resist more to the laser heating effect than the other samples that contains Y^{3+} ions with lower ionic size.

In view of the results summarized in Table 3, it is obviously seen that at low laser excitation power density (20 W cm^{-2}), the optimal S_r values are almost equal to 1.2 % K^{-1} (at 303 K) for all the studied compounds. However, at a higher excitation power density of 155 W cm^{-2}, it is clear that they are widely different from each other and they rise from 0.616 (at 313 K) to 1.136 % K^{-1} (at 303 K), respectively, for the Er^{3+}, Yb^{3+}: $Y_{0.79}VO_4$ and Er^{3+}, Yb^{3+}: $Gd_{0.79}VO_4$ MCs. Under both laser excitation power densities used, the best relative sensitivities were achieved at RT by the Er^{3+}, Yb^{3+}: $Gd_{0.79}VO_4$ compound with values of 1.207 % K^{-1} (at 20 W cm^{-2}) and 1.136 % K^{-1} (at 155 W cm^{-2}).

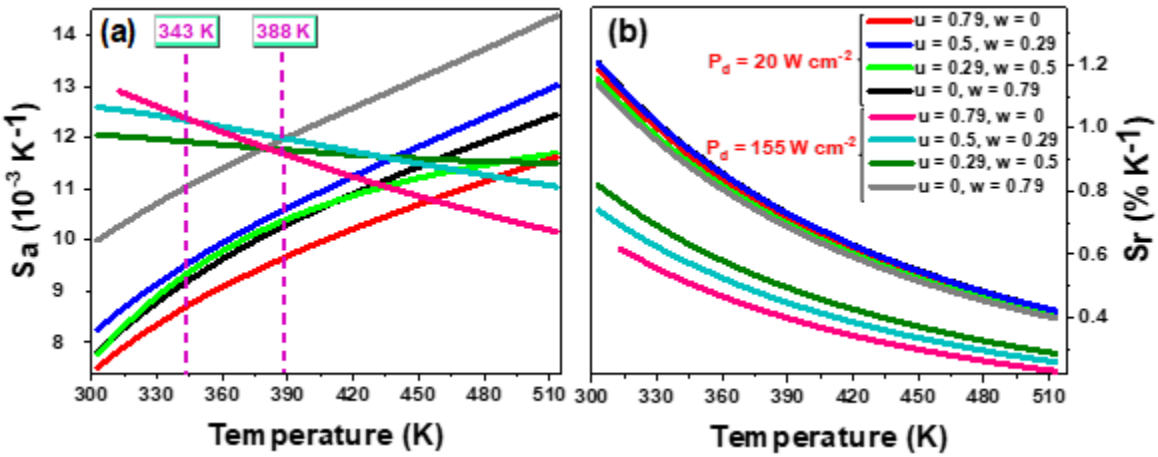

Fig. 9. Evolution of the thermometric parameters calculated for the Er^{3+}, Yb^{3+}: $Y_uGd_wVO_4$ MCs in the 303-513 K temperature range operated under 980 nm at two different excitation laser power densities of 20 and 155 W cm^{-2}: (a) absolute thermal sensitivity, and (b) relative thermal sensitivity.

The highest absolute thermal sensitivity of the luminescent-sensor materials we prepared was achieved by the Er^{3+}, Yb^{3+}: $Gd_{0.79}VO_4$ MCs excited at 155 W cm^{-2}, with the value of 14.373 10^{-3}

K^{-1} at 513 K. This value is better than those reported in the literature for other materials. Such as, it is almost the double than the one reported by Savchuk *et al.* (6.9 10^{-3} K^{-1}) for Er, Yb: $GdVO_4$ nanoparticles excited at 980 nm and analyzed in the 297- 343 K temperature range [36]. Also, it is significantly higher than those reported for Er, Yb: $GdVO_4$ (8.5 10^{-3} K^{-1}), Er, Yb: $GdVO_4$@SiO_2 (10.1 10^{-3} K^{-1}), Er, Yb: YVO_4 (10.5 10^{-3} K^{-1}), and Er, Yb: YVO_4 (11.69 10^{-3} K^{-1}) analyzed in the 307-473 K, 297-343 K, 320-598 K and 302-483 K temperature ranges, respectively [36,37-38,63]. Meanwhile, the optimal relative thermal sensitivity obtained by the Er^{3+}, Yb^{3+}: $Gd_{0.79}VO_4$ MCs excited at 20 W cm^{-2} with a value of 1.207 % K^{-1} at 303 K is similar to those reported for Er: YVO_4 (1.23 % K^{-1} at 300 K), Er, Yb: YVO_4 (1.178 % K^{-1} at ~293 K), Er, Yb: $GdVO_4$ (1.11 % K^{-1} at 307 K), Er, Yb: $GdVO_4$@SiO_2 (0.94 % K^{-1} at 343 K), and Er, Yb: YVO_4 (0.919 % K^{-1} at 302 K) [36-37,63-65]. Also, it is almost double the one reported by Singh *et al.* for Er, Yb: YVO_4 (0.584 % K^{-1} at 320 K) [38]. The comparison of the obtained data for the thermometric performance, in terms of sensitivity, with those reported in the literature, suggests that the luminescence thermometers we prepared would provide a higher accuracy.

According to equation (4), using the above obtained S_r values and the sensitivity of the detection system (0.5 %) [62], the temperature resolutions (δT) of all the analyzed sensors have been determined, and their variations in the 303-513 K temperature range and at the two different excitation power densities used (20 and 155 W cm^{-2}) have been presented in Fig. 10. Their optimal values are shown in Table 3.

The δT values determined for all the analyzed sensors fall in the 0.413 K (at 303 K)-2.178 K (at 513 K) interval, respectively, for Er^{3+}, Yb^{3+}: $Gd_{0.79}VO_4$ excited at 20 W cm^{-2} and for Er^{3+}, Yb^{3+}: $Y_{0.79}VO_4$ excited at 155 W cm^{-2}.

According to equation (4), the thermal resolution can be read as the inverse of the relative thermal sensitivity multiplied by a constant factor characterizing the detection system used, which is 0.5 % [62]. Thus, it is expected that the thermal resolution will behave as the inverse of the relative thermal sensitivity and will depend on the same factors as those on which S_r depends. In fact, one would be expected that the δT values will be almost the same at low excitation power density (20 W cm^{-2}) which is not the same case for higher excitation power density (155 W cm^{-2}). Even, the δT values determined at low pump power density (20 W cm^{-2}) will always remain lower than those determined at higher pump power density (155 W cm^{-2}). This expectation is well confirmed by Fig. 10 representing the evolution of δT with temperature for all the analyzed samples excited at 20 and 155 W cm^{-2}, such as it is obviously seen that δT increases monotonously as the temperature increases. Following the same reasoning as for S_r, at each given temperature, the δT values are almost the same for all the analyzed sensors excited at 20 W cm^{-2}. While, with exciting at 155 W cm^{-2}, they became widely different from each other depending on the atomic concentration of Gd^{3+} ions inserted in the rare earth vanadate host. Such as, as much as the atomic concentration of Gd^{3+} ions is higher as much as the thermal resolution of the sensor is more efficient. Then, at higher excitation pump power density of 155 W cm^{-2}, the thermal resolution shows an important dependence on the atomic concentration of Gd^{3+} ions and it could be enhanced whenever the concentration of Gd^{3+} has increased. In fact, at 155 W cm^{-2}, the decrease of the crystal field effect may lead to a better thermal resolution of the studied sensors, which is not the same case for lower excitation pump power density (20 W cm^{-2}) where any essential difference for several Gd^{3+} concentration can be found. Indeed, the efficient δT for all the analyzed sensors have been obtained under low excitation power density of 20 W cm^{-2}. Nevertheless, the Er^{3+}, Yb^{3+}: $Gd_{0.79}VO_4$ compound excited at 155 W cm^{-2} shows values that are nearly equal to those of analyzed sensors excited at 20 W cm^{-2}. Since the δT depends on the same factors as those on which S_r depends, then the use of rare earth ions with larger ionic size in the bases of the studied host may reduce the importance of the non-radiative depopulation processes and guarantee a better Boltzmann distribution population between the TCLs, which could enhance greatly the δT.

Regarding to the results presented in Table 3, it can be seen that the optimal δT values obtained at low excitation power density of 20 W cm^{-2} are around 0.42 K (at 303 K) for all the studied compounds. However, at a higher excitation power density of 155 W cm^{-2}, it decreases from 0.811 K (at 313 K) to 0.439 K (at 303 K) for the Er^{3+}, Yb^{3+}: $Y_{0.79}VO_4$ and Er^{3+}, Yb^{3+}: $Gd_{0.79}VO_4$ MCs, respectively. For both laser excitation power densities used, 20 and 155 W cm^{-2}, the efficient thermal

resolutions have been reached at RT by the Er^{3+}, Yb^{3+}: $Gd_{0.79}VO_4$ compound with values of 0.413 K and 0.439 K, respectively.

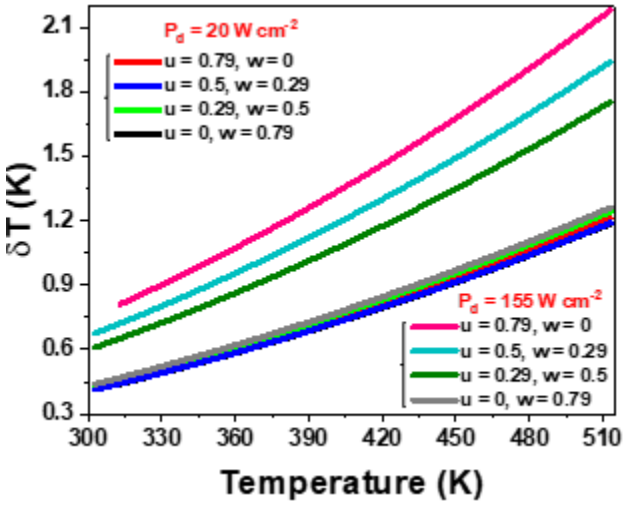

Fig. 10. Evolution of the thermal resolution calculated for the Er^{3+}, Yb^{3+}: $Y_uGd_wVO_4$ MCs in the 303-513 K temperature range operated under 980 nm at two different excitation laser power densities of 20 and 155 W cm^{-2}.

Table 3. Comparison between the experimental and numerical thermometric parameters of several FIR-based luminescent thermometers based on Er^{3+}, Yb^{3+}: $Y_uGd_wVO_4$ MCs in the 303-513 K temperature range operated under 980 nm at two different excitation laser power densities of 20 and 155 W cm^{-2}, using the green emissions of Er^{3+} ions.

Luminescence thermometers	Power density (W cm^{-2})	S_a (10^{-3} K^{-1})	S_a^{TS} (10^{-3} K^{-1})	S_r (% K^{-1})	S_r^{TS} (% K^{-1})	δT (K)
Er^{3+}, Yb^{3+}: $Y_{0.79}VO_4$	20	11.621 (513 K)	12.337 (513 K)	1.184 (303 K)	1.259 (303 K)	0.422 (303 K)
	155	12.901 (313)	14.275 (333 K)	0.616 (313 K)	0.699 (313 K)	0.811 (313 K)
Er^{3+}, Yb^{3+}: $Y_{0.5}Gd_{0.29}VO_4$	20	13.009 (513)	13.414 (513 K)	1.205 (303 K)	1.254 (303 K)	0.414 (303 K)
	155	12.593 (303)	13.776 (363 K)	0.738 (303 K)	0.796 (303 K)	0.676 (303 K)
Er^{3+}, Yb^{3+}: $Y_{0.29}Gd_{0.5}VO_4$	20	11.692 (513)	12.996 (513 K)	1.153 (303 K)	1.218 (303 K)	0.433 (303 K)
	155	12.060 (303)	13.018 (393 K)	0.817 (303 K)	0.848 (303 K)	0.611 (303 K)
Er^{3+}, Yb^{3+}: $Gd_{0.79}VO_4$	20	12.444 (513K)	11.949 (503 K)	1.207 (303 K)	1.202 (303 K)	0.413 (303 K)
	155	14.373 (513)	15.205 (513 K)	1.136 (303 K)	1.196 (303 K)	0.439 (303 K)

Furthermore, in order to determine the impact of the Gd^{3+} ion concentration on the optical heating of the sample induced by the laser excitation (980 nm) and emission processes, the FIR ratio of $^2H_{11/2} \rightarrow {}^4I_{15/2}$ versus $^4S_{3/2} \rightarrow {}^4I_{15/2}$ has been calculated over the whole excitation pump power density range of this study (20- 445 W cm^{-2}) for all the studied samples, using the integral area of each manifold of Fig. 5. The pump power density dependence of the FIR ratio between the two green observed emissions is shown in Fig. 11(a). It can be seen that by increasing the pump power density

from 20 to 445 W cm^{-2}, the FIR (I_H/ I_S) values increase exponentially for all the studied samples. The same patterns are observed in case of FIR vs. temperature graph for excitation pump power densities of 20 and 155 W cm^{-2} (Fig. 8(a)). This may indicate that the sample temperature depends strongly on the excitation pump power density used. The lower the concentration of the Gd^{3+} ion, the higher the slope of the FIR curve (see Fig. 11(a)). FIR can increase when the sample temperature increases, then it might be inferred that the laser excitation induced the heating of the studied samples. Therefore, as discussed previously in the literature by Sinha *et al.* and Pandey *et al.*, the obtained FIR values at different pump power densities can significantly be correlated with the FIR vs. temperature graph [66-67]. The temperature gained by the sample due to laser excitation for different Gd^{3+} concentrations can be calculated using equation (1) by determining T as a function of FIR [66-67]:

$$T = \left(\frac{\Delta E}{k_B}\right)\left[\frac{1}{\ln(B) - \ln(FIR)}\right] \qquad (6)$$

Going back to the admitted previous conclusion (in *Section 3.3.1*), obtaining a ΔE_{FIR} value closer to the experimental one, ΔE`, could be explained because the sample is less heated by the laser excitation. Then, here, we are going to use the ΔE_{FIR} and B_{FIR} values determined from the temperature sensing study for all the studied samples excited at 20 W cm^{-2}. The sample temperatures due to laser induced heating for the different Gd^{3+} concentrations could be determined and the dependence of their values on the excitation pump power density is presented in Fig. 11(b).

For all the studied samples, the generated temperature increases gradually when increasing the pump power density from 20 to 445 W cm^{-2}. Heat generation is maximum for the lowest Gd^{3+} (0 at. %) doping concentration and its value decreases as the concentration of this ion increases. Also, the higher the pump power density, the higher the heat generation as the Gd^{3+} concentration decreases. The main reason for the heat generated in the samples is the involvement of non-radiative transitions [66]. Thus, we can conclude that the increase of the Gd^{3+} concentration minimizes the laser induced heating in the studied samples, and then improves the thermometric performance of the luminescent T-sensors developed.

Considering the two pump power density values used for the thermometric performance study (20 and 155 W cm^{-2}), it appears that for the lower pump power density, the heat generation is very weak, while, by increasing the pump power density to 155 W cm^{-2}, the heat generation becomes significant (see Fig. 11(b)). Therefore, it is expected that the temperature measurement accuracy of all the studied samples at low pump power density will not be affected by the laser excitation. However, at higher pump power densities, several non-radiative transition processes will be produced due to laser excitation heating. Thus, under these conditions, even the measurement of a low temperature closer to the RT, the accuracy of the thermometric performance will be reduced, yielding to lower relative thermal sensitivities and temperature resolutions, as has been already proved in the discussions of Fig. 9(b) and Fig. 10. Moreover, it has been found that for the highest concentration of Gd^{3+} analyzed in this work, the relative thermal sensitivity and temperature resolution have not been significatively affected by the increase of the excitation pump power density, and their values remain closer to the ones obtained at low pump power densities.

These results also support that, under low excitation pump power densities, the FIR changes follow strictly the Boltzmann distribution law which could enhance the thermometric performance. However, at higher excitation pump power densities, the non-radiative depopulation of the excited states play a dominant role yielding to a deterioration of the thermometric performance. Furthermore, as already a comparison discussion has been introduced in *Section 3.1* about Fig. 2, the effect of the increase of the Gd^{3+} doping concentration on the thermometric sensitivity is associated to the decrease of the interaction probability with longer Er^{3+}-Er^{3+} distances in association with the increased of ionic radius of Gd^{3+} in comparison with Y^{3+}. Thus, to summarize, to get a better thermometric performance, it is important to use low pump power density excitations, and to use a higher Gd^{3+} concentration at the expense of Y^{3+} ions.

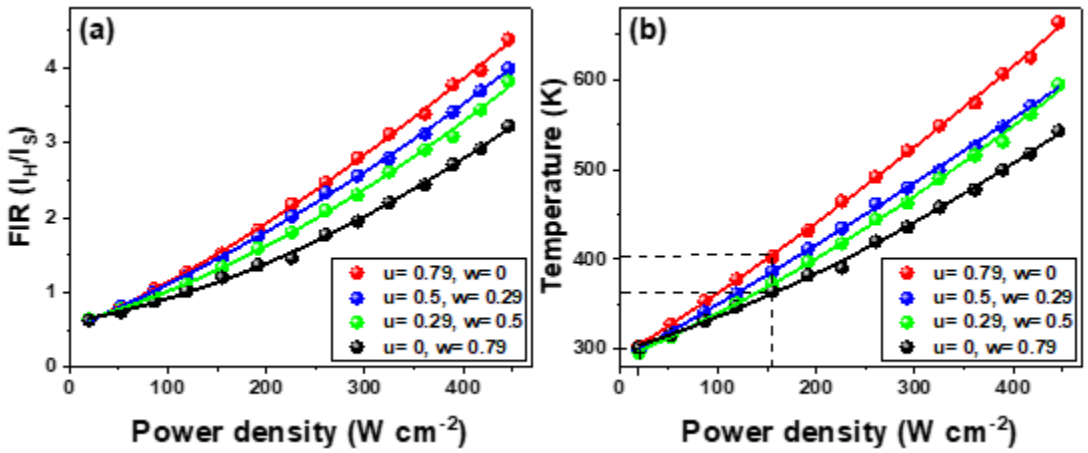

Fig. 11. (a) Dependence of the room temperature FIR of $^2H_{11/2}\rightarrow{}^4I_{15/2}$ versus $^4S_{3/2}\rightarrow{}^4I_{15/2}$ with the excitation pump power density for the Er^{3+}, Yb^{3+}: $Y_uGd_wVO_4$ MCs excited at 980 nm in the 20-445 W cm^{-2} excitation power density range. (b) Temperature changes of the Er^{3+}, Yb^{3+}: $Y_uGd_wVO_4$ phosphors excited at 980 nm versus the excitation pump power density.

3.4. Numerical thermometric performance parameters of Er^{3+}, Yb^{3+}: $Y_uGd_wVO_4$ MCs under anti-Stokes processes determined using TeSen tool.

TeSen Calculator is a numerical program, developed by Kaczmarek *et al.* on 2018 using Matlab software [68]. It is able to calculate the thermometric sensing parameters; in terms of the thermometric parameter FIR, and of the relative and absolute sensitivities; for any kind of ratiometric sensor material based on the steady state intensity change of two-emission peaks [68]. In the previous section, we have reported and discussed the thermometric parameter results of the prepared Er^{3+}, Yb^{3+}: $Y_uGd_wVO_4$ MCs calculated using the OriginLab@software. Here we are going to use the TeSen Calculator tool to determine them and we will present a comparison between the results obtained from both of these methods of calculation.

To evaluate numerically the luminescence ratiometric thermometers of Er^{3+}, Yb^{3+}: $Y_uGd_wVO_4$ MCs excited under an excitation laser wavelength of 980 nm with 20 and 155 W cm^{-2} as excitation pump power densities, we have used the same luminescence emission spectra measured over the 303-513 K temperature range with an increment of 10 K shown in Fig. 7 and the TeSen Calculator program.

Using the TeSen tool, the thermometric parameter FIR has been calculated using the integrated surface areas under the peaks attributed to the $^2H_{11/2}\rightarrow{}^4I_{15/2}$ and $^4S_{3/2}\rightarrow{}^4I_{15/2}$ transitions of Er^{3+} ions and based on Model 1 described on the numerical program as below [68]:

$$D = a\ exp\left(-\frac{e}{T}\right) \qquad (7)$$

Such as *D* corresponds to the FIR integral area ratio of $^2H_{11/2}\rightarrow{}^4I_{15/2}$ versus $^4S_{3/2}\rightarrow{}^4I_{15/2}$, a corresponds to the pre-exponential factor, *e* represents the value of the energy gap between the two thermalized levels of Er^{3+} ions (ΔE^{TS}) divided by the k_B Boltzmann's constant and *T* represents the absolute temperature.

Using the experimental spectra shown in Fig. 7 and the TeSen Calculator program, the FIR ratio of $^2H_{11/2}\rightarrow{}^4I_{15/2}$ versus $^4S_{3/2}\rightarrow{}^4I_{15/2}$, as expressed in equation (7), has been calculated for each temperature of study and each excitation laser power density used (20 and 155 W cm^{-2}). The evolution of the numerical FIR fit with temperature for the Er^{3+}, Yb^{3+}: $Y_uGd_wVO_4$ MCs, calculated using the TeSen tool together with the experimental FIR fit curves determined using OriginLab@software and equation (1), operated under anti-Stokes condition with pumping at the two different excitation power densities are depicted in Fig. 12.

It is obviously seen that the numerical FIR fit data have the same tendency followed by the experimental ones discussed as well previously in ***Section 3.3.1*** (see Fig. 12). With exciting at 20 W cm^{-2} and in the 303-513 K temperature range, all the numerical FIR fit data are nearly overlapped to each other and to the experimental ones. With exciting at 155 W cm^{-2}, at and closer to RT, the numerical data are nearly overlapped with the experimental ones. While, at higher temperatures, they overestimate the experimental ones but the difference between their values still not that much considerable for all the studied compounds. Taking into consideration the expressions of the absolute and relative sensitivities (equations (2) and (3)), the TCLs of Er^{3+} ions must own numerical absolute and relative sensitivity values (obtained with the TeSen Calculator program: S_a^{TS} and S_r^{TS}) similar or nearly equal to the experimental ones (obtained by OriginLab@software: S_a and S_r).

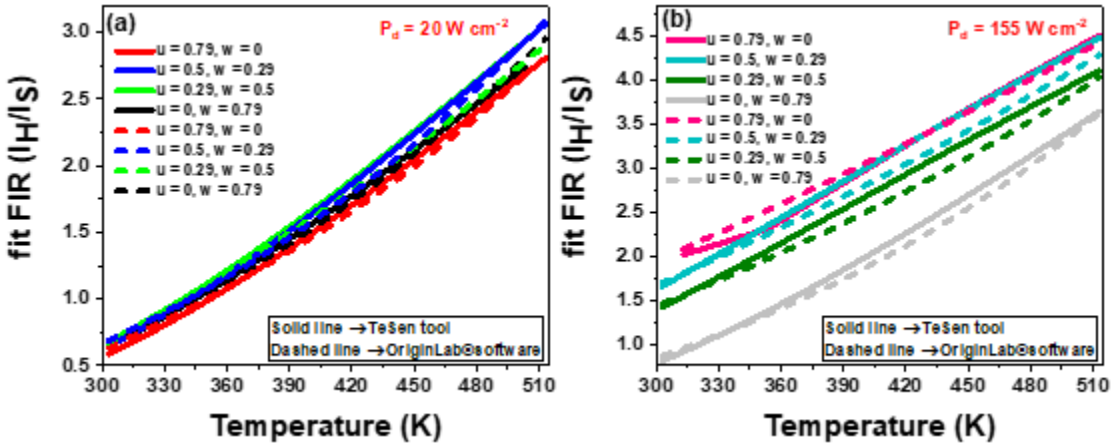

Fig. 12. The plot of the corresponding fitting according to the Boltzmann distribution low (described in its form: $FIR = B\ exp\left(-\frac{\Delta E}{k_B T}\right)$) of the integrated fluorescence intensity ratio of the Er^{3+} green anti-Stokes emissions for the I_H/I_S transitions as a function of temperature in the 303-513 K temperature range, for the Er^{3+}, Yb^{3+}: $Y_uGd_wVO_4$ MCs excited at two different excitation power densities. (a) at 20 W cm^{-2} and (b) at 155 W cm^{-2}. Solid lines show data determined using the TeSen Calculator tool and dashed lines shows data determined using OriginLab@software.

For all the different samples excited at the two different pump power densities (20 and 155 W cm^{-2}), the numerical energy gap (ΔE^{TS}) as well as the pre-exponential factor (*a*) could be easily deduced from the TeSen tool after fitting the FIR data following equation (7). The obtained values of a and ΔE^{TS} for all the prepared MCs are listed in Table 2.

It is obviously seen that for all the studied Er^{3+}, Yb^{3+}: $Y_uGd_wVO_4$ compounds the a and ΔE^{TS} values determined at low pump power density (20 W cm^{-2}) always remain greater than those determined at higher pump power density (155 W cm^{-2}). Except for the Er^{3+}, Yb^{3+}: $Gd_{0.79}VO_4$, a at 155 W cm^{-2} is higher than that at 20 W cm^{-2}. At low excitation power density of 20 W cm^{-2}, the obtained a and ΔE^{TS} values are almost the same for all the studied compounds and they fall in the 24.6-28.9 and 767-804 cm^{-1} ranges, respectively. At high excitation power density of 155 W cm^{-2}, they increase slightly from a sample to another one with higher atomic concentration of Gd^{3+} ions. Nevertheless, they show an obvious increment from 18.1 and 476 cm^{-1} for the Er^{3+}, Yb^{3+}: $Y_{0.79}VO_4$ to 30.9 and 763 cm^{-1} for the Er^{3+}, Yb^{3+}: $Gd_{0.79}VO_4$, respectively, for the a and ΔE^{TS} parameters. In comparison with the fitted obtained parameters, the a and ΔE^{TS} values are slightly overestimating the B_{FIR} and ΔE_{FIR} values for both cases of excitation pump power densities, except for the Er^{3+}, Yb^{3+}: $Gd_{0.79}VO_4$ excited at 20 W cm^{-2}, they are roughly equal. In addition, for both cases (low and high pump power densities), the ΔE^{TS} value underestimate the ΔE` experimental energy gap value (see Table 2).

Considering the equation (2), it could be seen how the absolute thermal sensitivity will also be affected by this ΔE^{TS} value, as well as the a pre-exponential factor. As Suo *et al.* indicated, when comparing the absolute sensitivity among different hosts, the pre-exponential factor will gain importance [69], then whenever, the ΔE^{TS} as well as the a values will be larger, the absolute sensitivity will be more efficient. Therefore, it will be an advance to conclude that the TeSen Calculator will give

us higher absolute sensitivity values in comparison with the ones obtained using OriginLab@software method in our samples.

According to the expression of the relative sensitivity (equation (3)), a larger energy gap between the TCLs benefits the enhancement of sensitivity [23]. Therefore, it will be an advance to conclude that the TeSen Calculator will give us slightly higher relative sensitivity values in comparison with the values obtained using the OriginLab@software method for all the studied compounds. Except for the Er^{3+}, Yb^{3+}: $Gd_{0.79}VO_4$ excited at 20 W cm^{-2}, the S_r^{TS} and S_r values will be rather the same at each given temperature in the 303-513 K whole temperature range of study. Moreover, at higher excitation power density (155 W cm^{-2}), the S_r^{TS} values will be rather the same for all the compounds, except for the Er^{3+}, Yb^{3+}: $Gd_{0.79}VO_4$ they will be larger.

Using this tool and taking into consideration the ratio of the integrated areas under the peaks attributed to the Er^{3+} green emissions, we have calculated the numerical S_a^{TS} and S_r^{TS} data points along for Model 1. Their evolutions with temperature in comparison with the experimental ones calculated using the OriginLab@software are presented in Fig. 13 and their maximum values are given in Table 3.

It is clearly seen that the numerical absolute and relative sensitivities have the same tendency followed by the experimental ones that they were well discussed in *Section 3.3.2*. Whatever the value of the excitation pump power density (20 or 155 W cm^{-2}), the numerical absolute and relative sensitivity values overestimate the experimental ones. Such as the difference between them remains very small (see Fig. 12). Meanwhile, the Er^{3+}, Yb^{3+}: $Gd_{0.79}VO_4$ excited at 20 W cm^{-2} shows S_r^{TS} and S_r data that are almost overlapped (see Fig. 13(c)). However, when it was excited at 155 W cm^{-2}, it shows obvious larger S_r^{TS} values in comparison with those of the studied compounds with lower concentration of Gd^{3+} ions that shows nearly equal values of S_r^{TS} at each given temperature (see Fig. 13(d)).

As revealed on Table 3, with pumping at 20 W cm^{-2}, the S_a^{TS} optimal values are nearly equal to the experimental S_a ones and they were found to be at the 513 K highest temperature. While, with pumping at 155 W cm^{-2}, their values still nearly equal to the experimental ones but they were not found at the same temperatures as that for S_a. Whatever the excitation pump power density used, the optimal values of the numerical S_r^{TS} are nearly equal to the experimental S_r ones and they were found closer to RT. In accordance with the experimental S_r, the optimal S_r^{TS} values are roughly equal to 1.2 % K^{-1} (at 303 K) for all the studied compounds excited at 20 W cm^{-2}. However, with exciting at 155 W cm^{-2}, they became widely different from each other with varying between 0.699 % K^{-1} (313 K) and 1.196 % K^{-1} (303 K).

The small difference on the thermometric parameter values between the numerical and the experimental methods used could be related once to the precision on the integrated area of peaks and to the goodness of the fit.

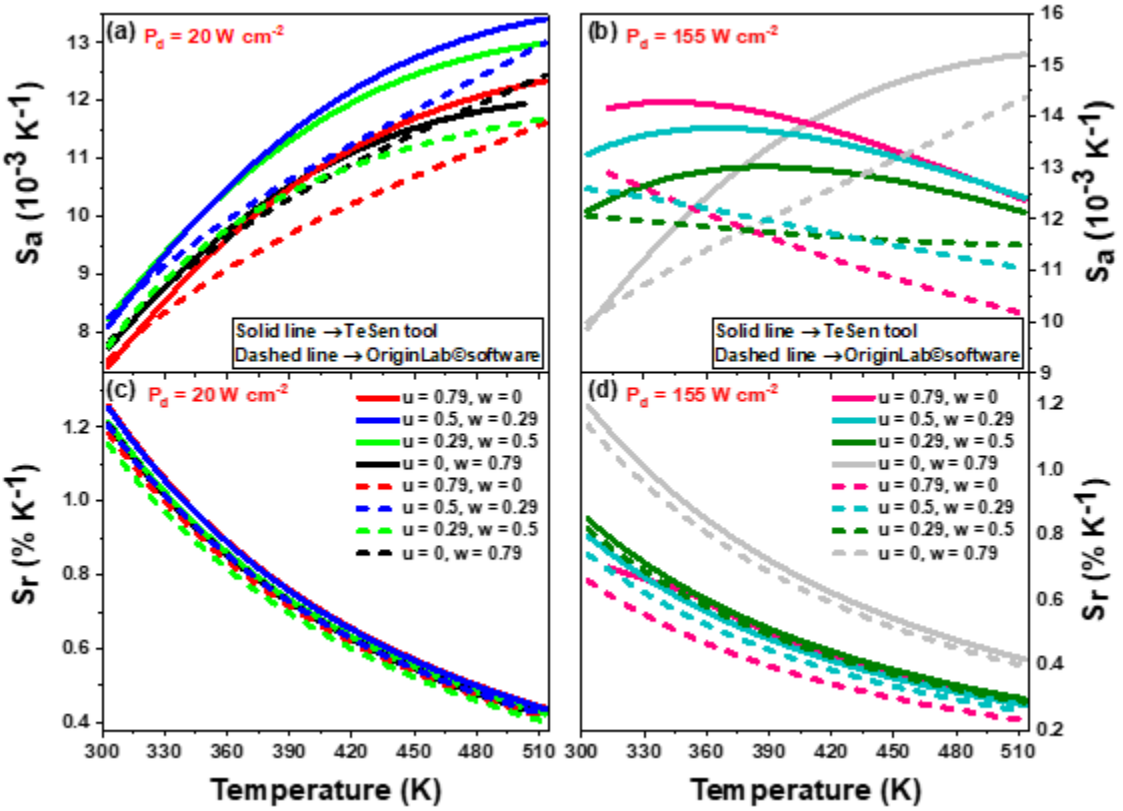

Fig. 13. Comparison between the numerical and the experimental thermometric parameters calculated for the Er^{3+}, Yb^{3+}: $Y_uGd_wVO_4$ MCs in the 303-513 K temperature range operated under 980 nm at two different excitation laser power densities of 20 and 155 W cm^{-2}: (a) and (b) relative thermal sensitivity, (c) and (d) absolute thermal sensitivity. Solid lines show data determined using the TeSen Calculator tool and dashed lines shows data determined using OriginLab@software.

4. Conclusion

Summarizing, we have investigated the influence of the excitation pump power density and the stoichiometry on the thermometric parameters of the Er^{3+}, Yb^{3+}: $Y_uGd_wVO_4$ developed luminescent thermometers that operate using FIR technique. We have compared the thermometric proprieties obtained at low and higher pump power densities of anti-Stokes excitation. We have also compared the results obtained using the OriginLab@software and the TeSen Calculator tool methods. It is well highlighted that whenever the value of the energy gap between the TCLs is closer to the experimental one, the luminescent thermometer will be more efficient. In addition, it was shown that the thermometric performance strongly depends on the excitation pump power density used and on the stoichiometry of the host material. Even in the non-saturation regime, a small rise in the excitation power density may affect largely the thermometric performances to be less powerful due to an extra-heating of the sample. Upon low excitation power density, the thermometric performances are approximately not affected by a small modification in the crystal field of the studied host as a thermometer. However, upon high excitation power density, due to the decrease of the crystal field effect, the increase of the atomic concentration of Gd^{3+} ions within the Er^{3+}, Yb^{3+}: $Y_uGd_wVO_4$ host plays a dominant role and is responsible for the enhancement of the thermometric parameters. The two methods of calculation used give a rise to similar or nearly equal thermometric performances. Such as at low excitation pump power density of 20 W cm^{-2}, the optimal values of relative thermal sensitivity and thermal resolution are rather equal for all the analyzed sensors and they found in the vicinity of 1.2 % K^{-1} and 0.42 K at 303 K, respectively. However, at higher excitation pump power density of 155 W cm^{-2}, they became widely different with moving from a sample to another one with higher atomic concentration of Gd^{3+} ions and they also found to be in the same vicinity as low pump power density, 1.2 % K^{-1} and 0.42 K at 303 K, respectively, for the Er^{3+}, Yb^{3+}: $Gd_{0.79}VO_4$ MCs.

References.

[1] F. Vetrone, R. Naccache, A. Zamarrón, A. J. de la Fuente, F. Sanz-Rodríguez, L. Martinez Maestro, E. M. Rodríguez, D. Jaque, J. G. Solé, J. A. Capobianco, Temperature Sensing Using Fluorescent Nanothermometers, ACS Nano. 4 (2010) 3254–3258. https://doi.org/10.1021/nn100244a.

[2] L. H. Fischer, G. S. Harms, O. S. Wolbeis, Upconverting Nanoparticles for Nanoscale Thermometry, Angew. Chem., Int. Ed. 50 (2011) 4546–4551. https://doi.org/10.1002/anie.201006835.

[3] B. Hildebrandt, P. Wust, O. Ahlers, A. Dieing, G. Sreenivasa, T. Kerner, R. Felix, H. Riess, The Cellular and Molecular Basis of Hyperthermia, Crit. Rev. Oncol. Hematol. 43 (2002) 33−56. https://doi.org/10.1016/S1040-8428(01)00179-2.

[4] J. L. R. Roti, Cellular Responses to Hyperthermia (40−46 degrees C): Cell Killing and Molecular Events, Int. J. Hyperthermia. 24 (2008) 3−15. https://doi.org/10.1080/02656730701769841.

[5] A. Siaï, P. Haro-González, K. Horchani-Naifer, M. Férid, La_2O_3: Tm, Yb, Er upconverting nano-oxides for sub-tissue lifetime thermal sensing, Sens. Actuators B Chem. 234 (2016) 541–548. https://doi.org/10.1016/j.snb.2016.05.019.

[6] Z. Sun, G. Liu, Z. Fu, T. Sheng, Y. Wei, Z. Wu, Nanostructured La_2O_3: Yb^{3+}/Er^{3+}: Temperature sensing, optical heating and bio-imaging application, Mater. Res. Bull. 92 (2017) 39–45. https://doi.org/10.1016/j.materresbull.2017.04.005.

[7] J. Wang, L. Luo, Y. Huang, W. Li, Effect of Yb Codoping on the Phase Transition, and Electrical and Photoluminescence Properties in KNLN:Er/xYb Ceramics, J. Am. Ceram. Soc. 99 (2016) 1625–1630. https://doi.org/10.1111/jace.14137.

[8] Y. Huang, L. Luo, Up-conversion photoluminescence based on the intrinsic defects in $Na_{0.5}Bi_{0.5}TiO_3$:Yb^{3+} ceramics, J. Alloys Compd. 706 (2017) 312–317. https://doi.org/10.1016/j.jallcom.2017.02.141.

[9] C. D. S. Brites, P. P. Lima, N. J. O. Silva, A. Millán, V. S. Amaral, F. Palacio, L. D. Carlos, Thermometry at the nanoscale, Nanoscale. 4 (2012) 4799–4829. https://doi.org/10.1039/C2NR30663H.

[10] D. Jaque, F. Vetrone, Luminescence nanothermometry, Nanoscale. 4 (2012) 4301–4326. https://doi.org/10.1039/C2NR30764B.

[11] X. D. Wang, O. S. Wolfbeis, R. J. Meier, Luminescent probes and sensors for temperature, Chem. Soc. Rev. 42 (2013) 7834-7869. https://doi.org/10.1039/C3CS60102A.

[12] V.K. Rai, Temperature sensors and optical sensors, Appl. Phys. B. 88 (2007) 297–303. https://doi.org/10.1007/s00340-007-2717-4.

[13] S.A. Wade, Temperature measurement using rare earth doped fibre fluorescence, phd, Victoria University, 1999. http://vuir.vu.edu.au/ (accessed April 2, 2021).

[14] S.A. Wade, S.F. Collins, G.W. Baxter, Fluorescence intensity ratio technique for optical fiber point temperature sensing, J. Appl. Phys. 94 (2003) 4743–4756. https://doi.org/10.1063/1.1606526.

[15] G. Xiang, X. Liu, Q. Xia, S. Jiang, X. Zhou, L. Li, Y. Jin, L. Ma, X. Wang. J. Zhang, Deep-Tissue Temperature Sensing Realized in BaY_2O_4:Yb^{3+}/Er^{3+} with Ultrahigh Sensitivity and Extremely Intense Red Upconversion Luminescence, Inorg. Chem. 59 (2020) 11054−11060. https://doi.org/10.1021/acs.inorgchem.0c01543.

[16] G. Xiang, Q. Xia, X. Liu, Y. Wang, S. Jiang, L. Li, X. Zhou, L. Ma, X. Wang, J. Zhang, Upconversion nanoparticles modified by Cu_2S for photothermal therapy along with real-time optical thermometry, Nanoscale 13 (2021) 7161−7168. https://doi.org/10.1039/D0NR09115D.

[17] H. Suo, X. Zhao, Z. Zhiyu, Y. Wu, C. Guo, Up-converting $LuVO_4$: $Nd^{3+}/Yb^{3+}/Er^{3+}@SiO_2@Cu_2S$ Hollow Nanoplatforms for Self-monitored Photothermal Ablation, ACS Appl. Mater. Interfaces 10 (2018) 39912−39920. https://doi.org/10.1021/acsami.8b18184.

[18] H. Suo, X. Zhao, Z. Zhang, C. Guo, Ultra-sensitive optical nano-thermometer $LaPO_4$: Yb^{3+}/Nd^{3+} based on thermo-enhanced NIR-to-NIR emissions, Chem. Eng. J. 389 (2020) 124506. https://doi.org/10.1016/j.cej.2020.124506.

[19] S. F. León-Luis, V. Monteseguro, U. R. Rodríguez-Mendoza, I. R. Martín, D. Alonso, J. M. Cáceres, V. Lavín, $2CaO{\cdot}Al_2O_3{:}Er^{3+}$ glass: An efficient optical temperature sensor, J. Lumin. 179 (2016) 272-279. https://doi.org/10.1016/j.jlumin.2016.07.005.
[20] S.F. Collins, G.W. Baxter, S.A. Wade, T. Sun, K.T.V. Grattan, Z.Y. Zhang, A.W. Palmer, Comparison of fluorescence-based temperature sensor schemes: Theoretical analysis and experimental validation, J. Appl. Phys. 84 (1998) 4649–4654. https://doi.org/10.1063/1.368705.
[21] H. Lu, H. Hao, G. Shi, Y. Gao, R. Wang, Y. Song, Y. Wang, X. Zhang, Optical temperature sensing in β-$NaLuF_4{:}Yb^{3+}/Er^{3+}/Tm^{3+}$ based on thermal, quasi-thermal and non-thermal coupling levels, RSC Adv. 6 (2016) 55307–55311. https://doi.org/10.1039/C6RA08311K.
[22] A. Sedlmeier, D.E. Achatz, L.H. Fischer, H.H. Gorris, O.S. Wolfbeis, Photon upconverting nanoparticles for luminescent sensing of temperature, Nanoscale. 4 (2012) 7090–7096. https://doi.org/10.1039/C2NR32314A.
[23] A.F. Pereira, K.U. Kumar, W.F. Silva, W.Q. Santos, D. Jaque, C. Jacinto, Yb^{3+}/Tm^{3+} co-doped $NaNbO_3$ nanocrystals as three-photon-excited luminescent nanothermometers, Sens. Actuators B Chem. 213 (2015) 65–71. https://doi.org/10.1016/j.snb.2015.01.136.
[24] Q. Zuo, L. Luo, Y. Yao, High Dielectric, Piezoelectric, Upconversion Photoluminescence and Low-Temperature Sensing Properties in $Ba_{0.7}Sr_{0.3}TiO_3$-$BaZr_{0.2}Ti_{0.8}O_3{:}Ho/Yb$ Ceramics, J. Electron. Mater. 45 (2016) 970–975. https://doi.org/10.1007/s11664-015-4247-x.
[25] D. Chen, M. Xu, S. Liu, X. Li, Eu^{2+}/Eu^{3+} dual-emitting glass ceramic for self-calibrated optical thermometry, Sens. Actuators B Chem. 246 (2017) 756–760. https://doi.org/10.1016/j.snb.2017.02.159.
[26] L. Marciniak, K. Prorok, A. Bednarkiewicz, Size dependent sensitivity of Yb^{3+},Er^{3+} up-converting luminescent nano-thermometers, J. Mater. Chem. C. 5 (2017) 7890–7897. https://doi.org/10.1039/C7TC02322G.
[27] K.-C. Liu, Z.-Y. Zhang, C.-X. Shan, Z.-Q. Feng, J.-S. Li, C.-L. Song, Y.-N. Bao, X.-H. Qi, B. Dong, A flexible and superhydrophobic upconversion-luminescence membrane as an ultrasensitive fluorescence sensor for single droplet detection, Light Sci. Appl. 5 (2016) e16136–e16136. https://doi.org/10.1038/lsa.2016.136.
[28] N. M. Bhiri, M. Dammak, M. Aguiló, F. Díaz, J. J. Carvajal, M. C. Pujol, Stokes and anti-Stokes operating conditions dependent luminescence thermometric performance of Er^{3+}-doped and Er^{3+}, Yb^{3+} co-doped $GdVO_4$ microparticles in the non-saturation regime, J. Alloys Compd. 814 (2020) 152197. https://doi.org/10.1016/j.jallcom.2019.152197.
[29] X. Xu, Z. Wang, P. Lei, Y. Yu, S. Yao, S. Song, X. Liu, Y. Su, L. Dong, J. Feng, H. Zhang, α-$NaYb(Mn)F_4{:}Er^{3+}/Tm^{3+}$@$NaYF_4$ UCNPs as “Band-Shape” Luminescent Nanothermometers over a Wide Temperature Range, ACS Appl. Mater. Interfaces. 7 (2015) 20813–20819. https://doi.org/10.1021/acsami.5b05876.
[30] H. Suo, C. Guo, T. Li, Broad-Scope Thermometry Based on Dual-Color Modulation up-Conversion Phosphor $Ba_5Gd_8Zn_4O_{21}{:}Er^{3+}/Yb^{3+}$, J. Phys. Chem. C. 120 (2016) 2914–2924. https://doi.org/10.1021/acs.jpcc.5b11786.
[31] B.S. Cao, Y.Y. He, Z.Q. Feng, Y.S. Li, B. Dong, Optical temperature sensing behavior of enhanced green upconversion emissions from Er–Mo: $Yb_2Ti_2O_7$ nanophosphor, Sens. Actuators B Chem. 159 (2011) 8–11. https://doi.org/10.1016/j.snb.2011.05.018.
[32] Y. Bai, Y. Wang, K. Yang, X. Zhang, Y. Song, C.H. Wang, Enhanced upconverted photoluminescence in Er^{3+} and Yb^{3+} codoped ZnO nanocrystals with and without Li^+ ions, Opt. Commun. 281 (2008) 5448–5452. https://doi.org/10.1016/j.optcom.2008.07.041.
[33] D. Chen, Z. Wan, Y. Zhou, Z. Ji, Cr^{3+}-doped gallium-based transparent bulk glass ceramics for optical temperature sensing, J. Eur. Ceram. Soc. 35 (2015) 4211–4216. https://doi.org/10.1016/j.jeurceramsoc.2015.08.005.
[34] A. Pandey, S. Som, V. Kumar, V. Kumar, K. Kumar, V.K. Rai, H.C. Swart, Enhanced upconversion and temperature sensing study of Er^{3+}–Yb^{3+} codoped tungsten–tellurite glass, Sens. Actuators B Chem. 202 (2014) 1305–1312. https://doi.org/10.1016/j.snb.2014.06.074.
[35] Y. Yang, C. Mi, F. Yu, X. Su, C. Guo, G. Li, J. Zhang, L. Liu, Y. Liu, X. Li, Optical thermometry based on the upconversion fluorescence from Yb^{3+}/Er^{3+} codoped La_2O_2S phosphor, Ceram. Int. 40 (2014) 9875–9880. https://doi.org/10.1016/j.ceramint.2014.02.081.
[36] O. A. Savchuk, J. J. Carvajal, C. Cascales, M. Aguiló, F. Díaz, Benefits of Silica Core–Shell Structures on the Temperature Sensing Properties of Er,Yb:$GdVO_4$ Up-Conversion

Nanoparticles, ACS Appl. Mater. Interfaces. 8 (2016) 7266–7273. https://doi.org/10.1021/acsami.6b01371.
[37] T.V. Gavrilović, D.J. Jovanović, V. Lojpur, M.D. Dramićanin, Multifunctional Eu^{3+}- and Er^{3+}/Yb^{3+}-doped $GdVO_4$ nanoparticles synthesized by reverse micelle method, Sci. Rep. 4 (2014). https://doi.org/10.1038/srep04209.
[38] A. K. Singh, P. K. Shahi, S. B. Rai, B. Ullrich, Host matrix impact on Er^{3+} upconversion emission and its temperature dependence, RSC Adv. 5 (2015) 16067–16073. https://doi.org/10.1039/C4RA12637H.
[39] Ł. Marciniak, A. Bednarkiewicz, D. Hreniak, W. Strek, The influence of Nd^{3+} concentration and alkali ions on the sensitivity of non-contact temperature measurements in $ALaP_4O_{12}:Nd^{3+}$ (A = Li, K, Na, Rb) nanocrystalline luminescent thermometers, J. Mater. Chem. C. 4 (2016) 11284–11290. https://doi.org/10.1039/C6TC03396B.
[40] L. Marciniak, K. Waszniewska, A. Bednarkiewicz, D. Hreniak, W. Strek, Sensitivity of a Nanocrystalline Luminescent Thermometer in High and Low Excitation Density Regimes, J. Phys. Chem. C. 120 (2016) 8877–8882. https://doi.org/10.1021/acs.jpcc.6b01636.
[41] B. Dong, R.N. Hua, B.S. Cao, Z.P. Li, Y.Y. He, Z.Y. Zhang, O.S. Wolfbeis, Size dependence of the upconverted luminescence of $NaYF_4$:Er,Yb microspheres for use in ratiometric thermometry, Phys. Chem. Chem. Phys. 16 (2014) 20009–20012. https://doi.org/10.1039/C4CP01966K.
[42] Y. Tian, Y. Tian, P. Huang, L. Wang, Q. Shi, C. Cui, Effect of Yb^{3+} concentration on upconversion luminescence and temperature sensing behavior in Yb^{3+}/Er^{3+} co-doped $YNbO_4$ nanoparticles prepared via molten salt route, Chem. Eng. J. 297 (2016) 26–34. https://doi.org/10.1016/j.cej.2016.03.149.
[43] R. Wang, X. Zhang, F. Liu, Y. Chen, L. Liu, Concentration effects on the FIR technique for temperature sensing, Opt. Mater. 43 (2015) 18–24. https://doi.org/10.1016/j.optmat.2015.02.015.
[44] L. Li, F. Qin, Y. Zhou, Y. Zheng, H. Zhao, Z. Zhang, Approximate energy gaps, dissimilar relative thermal sensitivities, Sens. Actuators B Chem. 269 (2018) 203–209. https://doi.org/10.1016/j.snb.2018.04.158.
[45] W. Xu, B. Chen, W. Yu, Y. Zhu, T. Liu, S. Xu, X. Min, X. Bai, H. Song, The up-conversion luminescent properties and silver-modified luminescent enhancement of $YVO_4:Yb^{3+}$, Er^{3+} NPs, Dalton Trans. 41 (2012) 13525–13532. https://doi.org/10.1039/C2DT31435E.
[46] N. M. Bhiri, M. Dammak, M. Aguiló, F. Díaz, J. J. Carvajal, M. C. Pujol, Excitation power dependence of a primary luminescent thermometer based on Er^{3+}, Yb^{3+}: $GdVO_4$ microcrystals operating in the visible, J. Alloys Compd. (submitted).
[47] M. G. Nikolić, D. J. Jovanović, M. D. Dramićanin, Temperature dependence of emission and lifetime in Eu^{3+}- and Dy^{3+}-doped $GdVO_4$, Appl. Opt. 52 (2013) 1716–1724. https://doi.org/10.1364/AO.52.001716.
[48] V. S. Hingwe, K. A. Koparkar, N. S. Bajaj, S. K. Omanwar, Optical properties of one-dimensional hybrid PVA/$YVO_4:Eu^{3+}$ nanofibers synthesized by electrospining, Optik. 140 (2017) 211–215. https://doi.org/10.1016/j.ijleo.2017.04.047.
[49] S. Tang, M. Huang, J. Wang, F. Yu, G. Shang, J. Wu, Hydrothermal synthesis and luminescence properties of $GdVO_4:Ln^{3+}$ (Ln=Eu, Sm, Dy) phosphors, J. Alloys Compd. 513 (2012) 474–480. https://doi.org/10.1016/j.jallcom.2011.10.093.
[50] R. D. Shannon, Revised effective ionic radii and systematic studies of interatomic distances in halides and chalcogenides, Acta Crystallogr. Sect. A. 32 (1976) 751–767. https://doi.org/10.1107/S0567739476001551.
[51] N. Tancret, DETERMINATION DE STRUCTURES AB INIT/0 PAR DIFFRACTION X SUR POUDRE: APPLICATION A QUELQUES OXYDES, (n.d.) 244.
[52] V. Muhr, M. Buchner, T. Hirsch, D.J. Jovanović, S.D. Dolić, M.D. Dramićanin, O.S. Wolfbeis, Europium-doped $GdVO_4$ nanocrystals as a luminescent probe for hydrogen peroxide and for enzymatic sensing of glucose, Sens. Actuators B Chem. 241 (2017) 349–356. https://doi.org/10.1016/j.snb.2016.10.090.
[53] W. J. Park, M. K. Jung, D. H. Yoon, Influence of Eu^{3+}, Bi^{3+} co-doping content on photoluminescence of YVO_4 red phosphors induced by ultraviolet excitation, Sens. Actuators B Chem. 126 (2007) 324–327. https://doi.org/10.1016/j.snb.2007.02.033.

[54] A. Tymiński, T. Grzyb, S. Lis, $REVO_4$-Based Nanomaterials (RE = Y, La, Gd, and Lu) as Hosts for Yb^{3+}/Ho^{3+}, Yb^{3+}/Er^{3+}, and Yb^{3+}/Tm^{3+} Ions: Structural and Up-Conversion, J. Am. Ceram. Soc. 99 (2016) 3300-3308. https://doi.org/10.1111/jace.14344.

[55] D. J. Jovanović, Ž. Antić, R. M. Krsmanović, M. Mitrić, V. Đorđević, B. Bártová, M.D. Dramićanin, Annealing effects on the microstructure and photoluminescence of Eu_{3+}-doped $GdVO_4$ powders, Opt. Mater. 35 (2013) 1797–1804. https://doi.org/10.1016/j.optmat.2013.03.012.

[56] H. Xin, L.-X. Lin, J.-H. Wu, B. Yan, Hydrothermal synthesis and multi-color photoluminescence of $GdVO_4$: Ln^{3+} (Ln = Sm, Dy, Er) sub-micrometer phosphors, J. Mater. Sci. Mater. Electron. 22 (2011) 1330–1334. https://doi.org/10.1007/s10854-011-0308-y.

[57] L. Yang, L. Li, M. Zhao, G. Li, Size-induced variations in bulk/surface structures and their impact on photoluminescence properties of $GdVO_4$:Eu^{3+} nanoparticles, Phys. Chem. Chem. Phys. 14 (2012) 9956–9965. https://doi.org/10.1039/C2CP41136A.

[58] J. B. Gruber, G. W. Burdick, S. Chandra, D.K. Sardar, Analyses of the ultraviolet spectra of Er_{3+} in Er_2O_3 and Er^{3+} in Y_2O_3, J. Appl. Phys. 108 (2010) 023109. https://doi.org/10.1063/1.3465615.

[59] L. Li, L. Zheng, W. Xu, Z. Liang, Y. Zhou, Z. Zhang, W. Cao, Optical thermometry based on the red upconversion fluorescence of Er^{3+} in $CaWO_4$:Yb^{3+}/Er^{3+} polycrystalline powder, Opt. Lett. 41 (2016) 1458–1461. https://doi.org/10.1364/OL.41.001458.

[60] J. Li, J. Yan, D. Wen, W. U. Khan, J. Shi, M. Wu, Q. Sua, P. A. Tanner, Advanced Red Phosphors for White Light-emitting Diodes, J. Mater. Chem. C 4 (2016) 8611-8623. https://doi.org/10.1039/C6TC02695H.

[61] Z. Wang, D. Ananias, A. Carné-Sánchez, C.D.S. Brites, I. Imaz, D. Maspoch, J. Rocha, L.D. Carlos, Lanthanide–Organic Framework Nanothermometers Prepared by Spray-Drying, Adv. Funct. Mater. 25 (2015) 2824–2830. https://doi.org/10.1002/adfm.201500518.

[62] O. A. Savchuk, J. J. Carvajal, C.D. S. Brites, L. D. Carlos, M. Aguilo, F. Diaz, Upconversion thermometry: a new tool to measure the thermal resistance of nanoparticles, Nanoscale. 10 (2018) 6602–6610. https://doi.org/10.1039/C7NR08758F.

[63] M. K. Mahata, K. Kumar, V. K. Rai, Er^{3+}–Yb^{3+} doped vanadate nanocrystals: A highly sensitive thermographic phosphor and its optical nanoheater behavior, Sens. Actuators B 209 (2015) 775–780. https://doi.org/10.1016/j.snb.2014.12.039.

[64] M. N. Getz, O. Nilsen, H. Per-Anders, Sensors for optical thermometry based on luminescence from layered YVO_4: Ln^{3+} (Ln = Nd, Sm, Eu, Dy, Ho, Er, Tm, Yb) thin films made by atomic layer deposition, Sci. Rep. 9 (2019). https://doi.org/10.1038/s41598-019-46694-8.

[65] Q. Meng, T. Liu, J. Dai, W. Sun, Study on optical temperature sensing properties of YVO4:Er^{3+}, Yb^{3+} nanocrystals, J. Lumin. 179 (2016) 633–638. https://doi.org/10.1016/j.jlumin.2016.07.002.

[66] S. Sinha, M. K. Mahata, K. Kumar, Up/down-converted green luminescence of Er^{3+}–Yb^{3+} doped paramagnetic gadolinium molybdate: a highly sensitive thermographic phosphor for multifunctional applications, RSC Adv. 6 (2016) 89642-89654. https://doi.org/10.1039/C6RA20332A.

[67] A. Pandey, V. K.r Rai, V. Kumar, V. Kumar, H.C. Swart, Upconversion based temperature sensing ability of Er^{3+}-Yb^{3+} codoped $SrWO_4$: An optical heating phosphor, Sens. Actuators B Chem. 209 (2015) 352-358. https://doi.org/10.1016/j.snb.2014.11.126.

[68] A. M. Kaczmarek, R. Van Deun, M. K. Kaczmarek, TeSen – tool for determining thermometric parameters in ratiometric optical thermometry, Sens. Actuators B Chem. 273 (2018) 696–702. https://doi.org/10.1016/j.snb.2018.06.086.

[69] H. Suo, C. Guo, J. Zheng, B. Zhou, C. Ma, X. Zhao, T. Li, P. Guo, E.M. Goldys, Sensitivity Modulation of Upconverting Thermometry through Engineering Phonon Energy of a Matrix, ACS Appl. Mater. Interfaces. 8 (2016) 30312–30319. https://doi.org/10.1021/acsami.6b12176.